JGR Oceans

RESEARCH ARTICLE
10.1029/2020JC016693

Trends and Transport Variability of the Circulation in the Subpolar Eastern North Atlantic

Hannah Nowitzki[1,2], Monika Rhein[1,2], Achim Roessler[1,2], Dagmar Kieke[1,2], and Christian Mertens[1]

[1]Institute of Environmental Physics, University of Bremen, Bremen, Germany, [2]MARUM—Center for Marine Environmental Sciences, University of Bremen, Bremen, Germany

Key Points:

- A direct northward pathway into the eastern subpolar North Atlantic was identified contributing 22% to the total inflow
- Interior meridional transport east of 31°W is anticorrelated with interior western basin flow and with transport across Mid-Atlantic Ridge
- The transport decline in western basin is partly compensated by long term trend east of 31°W

Correspondence to:
H. Nowitzki,
h.nowitzki@uni-bremen.de

Citation:
Nowitzki, H., Rhein, M., Roessler, A., Kieke, D., & Mertens, C. (2021). Trends and transport variability of the circulation in the subpolar eastern North Atlantic. *Journal of Geophysical Research: Oceans*, *126*, e2020JC016693. https://doi.org/10.1029/2020JC016693

Received 6 AUG 2020
Accepted 14 JAN 2021

Abstract The North Atlantic Current is the major pathway for warm and saline water from the subtropics into the subpolar North Atlantic. Its main branch crosses 47°/48°N in the western North Atlantic basin and further north the Mid-Atlantic Ridge (MAR) before entering the eastern subpolar basin where it partly feeds the subpolar gyre. To quantify the meridional exchange of water between the subtropical and subpolar regime in the interior eastern North Atlantic, long-term (1993–2017) transport time series were calculated by combining data from inverted echo sounders taken in 2016–2017 with the dynamic topography from satellite altimetry. The data reveal an additional more direct pathway from the south across 47°/48°N with a mean northward transport of 9.1 Sv ± 0.8 Sv contributing about 22% to the total inflow of 41.4 Sv into the eastern subpolar basin. The transport time series of this pathway is significantly anticorrelated to the zonal transport across the MAR ($R = -0.7$), damping the interannual variability of the total transport into the subpolar eastern North Atlantic. Moreover, for the meridional transport in the interior eastern basin, a positive trend of 2.0 Sv ± 1.5 Sv per decade is found, partly balancing the negative decadal trend of −6.0 Sv ± 5.7 Sv observed in the interior western basin.

Plain Language Summary Within the North Atlantic Current, warm and salty water is transported from the subtropics into the subpolar North Atlantic. The well-studied main branch of this ocean current crosses the latitude of 47°/48°N in the western North Atlantic, turns eastward further north and crosses the Mid-Atlantic Ridge (MAR), before entering the eastern subpolar basin. By combining data from moored instruments with satellite observations, we calculate how much water is transported north- and southward across 47°/48°N in the interior eastern basin. In addition to the well-known pathway into the subpolar eastern basin crossing the MAR further north, our data reveal a more direct pathway from the south crossing 47°/48°N in the eastern basin. This pathway contributes 22% to the total inflow into the subpolar eastern basin. The two pathways into the eastern subpolar basin are anticorrelated: the strength of the flow across the MAR decreases when the northward flow in the eastern basin across 47°/48°N increases and vice versa. Moreover, the northward flow across 47°/48°N in the interior eastern basin has increased since 1993 while the flow across 47°/48°N in the western basin has decreased.

1. Introduction

The North Atlantic Current (NAC) as a northward extension of the Gulf Stream transports warm and saline water from the subtropics into the subpolar North Atlantic (Rossby, 1996). It forms the upper limb of the Atlantic Meridional Overturning Circulation (AMOC) and as such plays an important role for the global climate (IPCC, 2014). In the Newfoundland Basin, the NAC splits up into a recirculation (Bower et al., 2009; Mertens et al., 2014) and different branches that cross the Mid-Atlantic Ridge (MAR) via the Charlie-Gibbs, Maxwell and Faraday Fracture Zones (Bower & von Appen, 2008; Rhein et al., 2011; Roessler et al., 2015). These branches subsequently flow eastward into the Nordic Seas or westward, contributing to the Subpolar Gyre (Figure 1a). Various studies exist that quantify the transports between the subtropical and subpolar regime in the Newfoundland Basin and the northward extending NAC branches crossing the MAR (among others Breckenfelder et al., 2017; Mertens et al., 2014; Rhein et al., 2011, 2019; Roessler et al., 2015) and several studies discuss the transports in the eastern Atlantic at the Greenland-Portugal OVIDE line (e.g. Breckenfelder et al., 2017; Daniault et al., 2016; Mercier et al., 2015). However, less studies exist concerning the meridional exchange of water between the subpolar and subtropical regime in the eastern basin.

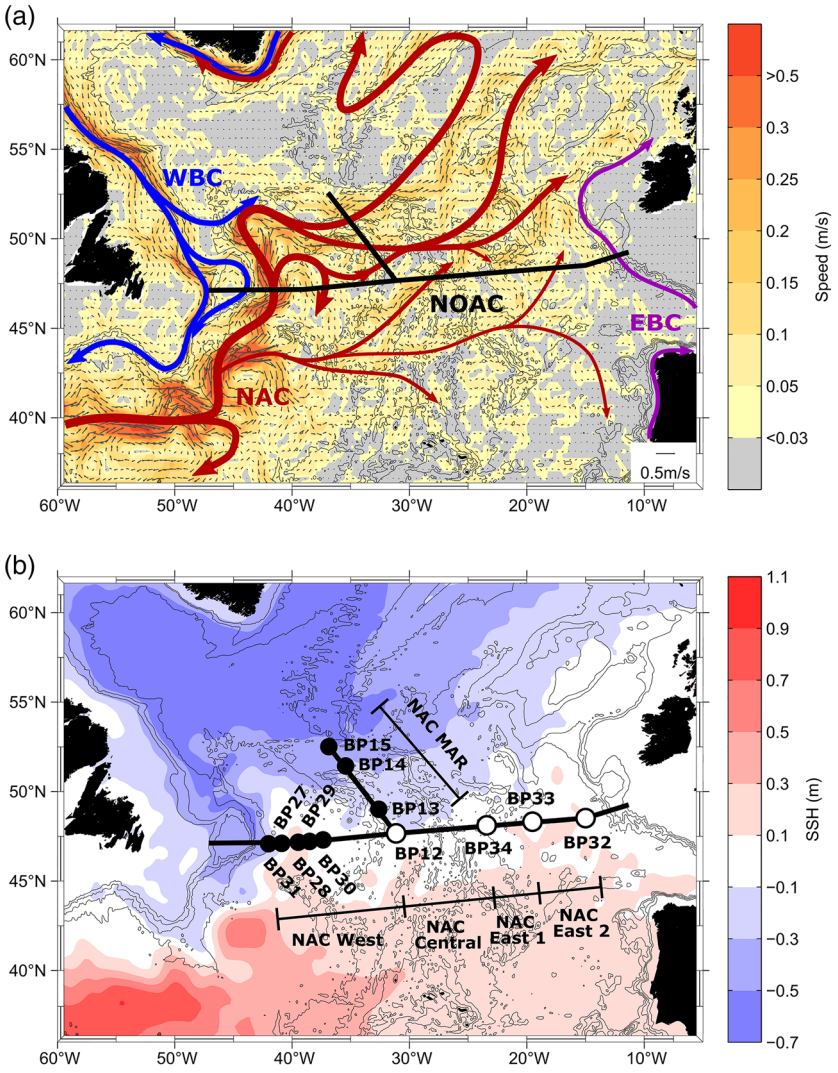

Figure 1. Panel (a) shows a simplified circulation scheme with a focus on the NAC and the location of the North Atlantic Changes (NOAC) array (e.g. Frajka-Williams et al., 2019). The colored contour plot in the background represents the mean satellite derived geostrophic surface velocity in 2016/2017, the arrows represent the direction and are scaled according to the velocity. The NAC circulation scheme is based on results of this study, previous studies (Daniault et al., 2016; Stendardo et al., 2020), and the satellite geostrophic velocity. The western boundary current as shown here combines the flow paths of the West Greenland Current, the Labrador Current and the Deep Western Boundary Current (Schneider et al., 2015). The eastern boundary current system (EBC) as shown here combines the flow paths of the Mediterranean Outflow Water and the slope current (Daniault et al., 2016; González-Pola et al., 2019, 2005; Holliday et al., 2015; Lozier & Stewart, 2008; Stendardo et al., 2015). Panel (b) shows a detailed view of the NOAC array including the PIES locations shown as black and white circles, the PIES names (BPXX), and defined transport sections: NAC MAR (47°40'N–53°N, transports analyzed in Roessler et al., 2015), NAC West/interior western basin (42°W–31°W, transports analyzed in Rhein et al., 2019), NAC Central (31°W–23°30'W), NAC East 1 (23°30'W–19°30'W) and NAC East 2 (19°30'W–15°W). The PIES represented by black circles are used in the SSH analysis. For the PIES represented by white circles, SSH and transports are analyzed. The colored contour plot represents the mean satellite SSH in 2016/2017. Both panels show the bathymetry with gray contour lines every 1000 m. NAC, North Atlantic Current; PIES, pressure sensor equipped inverted echo sounders; SSH, sea surface height.

It is thought that the inflow of subtropical water into the eastern subpolar basin occurs through the zonal transport from the western basin across the MAR (e.g. García-Ibáñez et al., 2015; Lherminier et al., 2010; Schmitz & McCartney, 1993; Schott et al., 2004). Combining PIES and Argo data with satellite altimetry, Roessler et al. (2015) observed a total transport of about 32 Sv (updated time series in McCarthy et al., 2020) crossing the MAR north of 47°40'N, and estimated that about 60% were of subtropical origin. The question

whether and how much other warm and saline water pathways exist that for instance cross the MAR further south and enter the subpolar eastern Atlantic by crossing 48°N is still open to discussion. Daniault et al. (2016, their Figure 9) used repeat hydrographic and ADCP data collected biannually between 2002 and 2012 at the OVIDE line which is located further east than the MAR at these latitudes and reported a larger transport than Roessler et al. (2015) and McCarthy et al. (2020), suggesting that a pathway south of 47°40'N exists. Another inflow into the subpolar eastern Atlantic contains warm and salty water from the Mediterranean Sea that flows through the Strait of Gibraltar and forms part of the northward flowing eastern boundary current system (e.g. Iorga & Lozier, 1999; Reid, 1979).

This study aims to elucidate the exchange of water between the subpolar and subtropical North Atlantic in the eastern basin across 47°/48°N from 31°W to 15°W, i.e. excluding the eastern boundary current system (Figure 1a). To obtain volume transport time series, we use data from moored pressure sensor equipped inverted echo sounders (PIES), combined with altimetry data, following the methods described in Rhein et al. (2019) and Roessler et al. (2015). The moored sensors contribute to the eastern part of the "North Atlantic Changes" (NOAC) instrumental array deployed along 47°/48°N (e.g. Frajka-Williams et al., 2019). Figure 1b indicates that the 47°/48°N section basically follows the transition zone between the subtropical and subpolar regime, expressed by generally low levels of sea surface height (SSH) elevations. Any noticeable meridional transport is thus interpreted as an exchange of volume between the two regimes. The water which is transported northward across the eastern part of the array presumably is to a large extent of subtropical origin. However, since we do not differentiate between the various water masses we cannot quantify the exact amount. In addition to the transport calculation, we present a comparison of the different NAC regimes in terms of barotropic and baroclinic SSH fluctuations.

To provide a first glimpse of the circulation near 47°/48°N, the mean meridional velocity in 2003–2017 obtained from repeat lowered acoustic Doppler current profiler (LADCP) measurements is presented in Figure 2. The flow is mainly surface intensified, with the strongest signals at the western boundary (Mertens et al., 2014; Rhein et al., 2019). In the eastern basin, the velocities are smaller, and in contrast to the western basin, no permanent features could be depicted from the individual LADCP sections, which might be partly owed to the much-reduced data coverage compared to the west. For later use, the

Table 1
Deployment Positions, Depths and Deployment Periods for the PIES

Name		Position	Water depth	Deployment period
PIES array western basin	BP31	47°05.84'N/41°59.94'W	4,236 m	25 May 2014–19 Jun 2017
	BP27	47°05.84'N/40°52.53'W	4,486 m	1 Jun 2013–22 Apr 2016
	BP28	47°09.68'N/39°30.06'W	4,578 m	31 May 2013–28 Apr 2016
	BP29	47°12.52'N/38°31.09'W	4,607 m	31 May 2013–27 Apr 2016
	BP30	47°17.52'N/37°21.47'W	4,546 m	31 May 2013–22 Apr 2016
PIES array MAR	BP12[a]	47°39.91'N/31°08.88'W	4,090 m	7 Aug 2006–19 Apr 2018
	BP13[a]	49°01.15'N/32°36.69'W	3,968 m	7 Aug 2006–28 May 2013
	BP14[a]	51°25.76'N/35°26.11'W	3,631 m	8 Aug 2006–6 Jun 2015
	BP15	52°30.48'N/36°51.63'W	3,386 m	9 Aug 2006–16 May 2014
PIES array eastern basin	BP32	48°31.12'N/15°00.22'W	4,796 m	7 Apr 2016–6 Jun 2017
	BP33	48°18.50'N/19°31.74'W	4,560 m	8 Apr 2016–8 Jun 2017
	BP34	48°06.60'N/23°25.32'W	4,486 m	10 Apr 2016–10 Jun 2017

Note. Whenever possible the position and depth were determined via trilateration. The deployment period does not necessarily correspond to the time period from which the data was analyzed. For positions that were equipped several times with an instrument, only the latest position/depth is shown. Details concerning the array in the western basin can be found in Rhein et al. (2019), details concerning the MAR array in Roessler et al. (2015).

MAR, Mid-Atlantic Ridge; PIES, pressure sensor equipped inverted echo sounders.

[a] Positions were not continuously equipped with instruments during the specified deployment period, and the time series exhibits gaps.

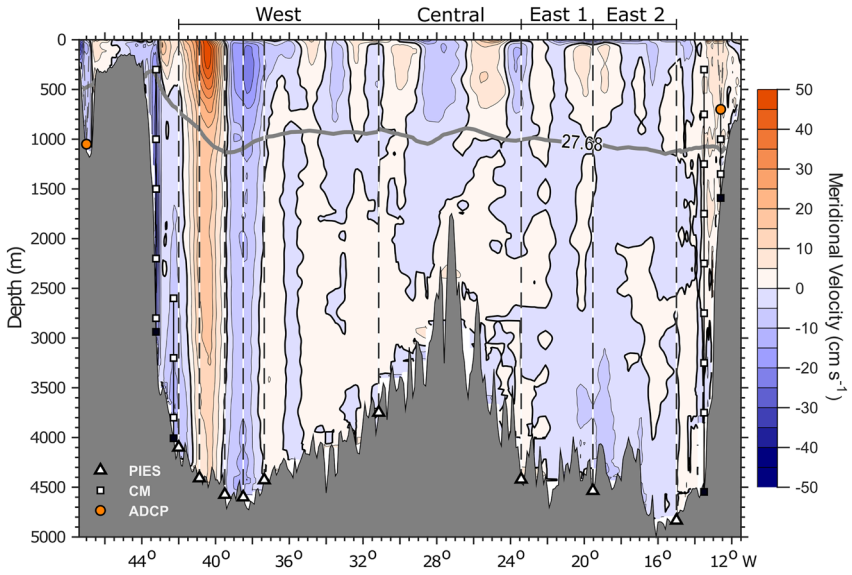

Figure 2. The NOAC array at 47°/48°N. Location of PIES (white triangles) and conventional deep-sea moorings at the western and eastern boundary with upward looking ADCPs (orange) and single point acoustic current meters (white squares). Colors denote the meridional velocities obtained from repeat lowered acoustic Doppler current profiler (LADCP) measurements (2003–2017). The line on top indicates the region where transports obtained from PIES observations are calculated and discussed, divided into a western, a central and two eastern segments. West of 44°W, the mean is calculated from on average 8 LADCP profiles, between 44°W and 31°W from on average 24, between 31°W and 15°W, from on average 8 profiles, and east of 15°W, from on average 4 profiles. Further information on the LADCP, western mooring and PIES data can be found in Mertens et al. (2014) and Rhein et al. (2019). NOAC, North Atlantic Changes; PIES, pressure sensor equipped inverted echo sounders.

transport study region is divided into a western, a central, and two eastern segments and the MAR region (Figures 1 and 2).

The study is organized as follows: After the presentation of the data, we explain the method to convert PIES measurements of bottom pressure fluctuations and acoustic travel times into time series of barotropic and baroclinic SSH and transport fluctuations. We furthermore discuss how baroclinic transport time series inferred from PIES data are made absolute using the mapped absolute dynamic topography (MADT) from altimeter data, and we use the high correlations between PIES and altimetry to extend the PIES transport time series back to 1993, the beginning of the altimeter record. The discussion highlights the characteristics and role of eastern basin transports in comparison to the circulation in the western basin and across the MAR, including long-term trends. In the appendix, uncertainty estimates concerning the calculated PIES transport time series are presented.

2. Data

This study builds on a variety of different observational data obtained from single-point measurements by moored devices, repeated ship surveys and large-scale remote sensing that are outlined in the following.

2.1. PIES

PIES are moored instruments, deployed at the seafloor, that measure bottom pressure and the vertical round trip travel time τ of an acoustic signal sent out by the PIES at a frequency of 12 kHz. This signal travels to the sea surface where it is reflected, and back to the instrument which records its arrival time (Chaplin & Watts, 1984; Watts & Rossby, 1977). Depending on the respective water depth at each instrument site, acoustic travel times are typically in the order of a few seconds. Measurements of bottom pressure, representing mass changes in the water column, are used to calculate the barotropic contribution to

Table 2
Research Cruises From Which CTD Data are Used to Create the Transfer Function for PIES BP12

Research vessel	Cruise	Date CTD stations	# Stations	DOI/Reference
Maria S. Merian	MSM43	9 Jun 2015–12 Jun 2015	10	10.2312/cr_msm43
Maria S. Merian	MSM53	14 Apr 2016–21 Apr 2016	16	10.2312/cr_msm53
Celtic Explorer	CE17007	13 May 2017	1	Personal communication. (cruise report: https://cchdo.ucsd.edu/data/14809/45CE20170427_do.pdf)
Maria S. Merian	MSM64	12 Jun 2017–13 Jun 2017	3	10.2312/cr_msm64
Maria S. Merian	MSM73	19 Apr 2018–17 May 2018	9	10.2312/cr_msm73

CTD, conductivity-temperature-depth; PIES, pressure sensor equipped inverted echo sounders.

SSH and transport fluctuations. Measurements of the acoustic travel time, representing density changes in the water column, are converted into the baroclinic contribution to SSH and transport fluctuations.

Throughout the past years, 12 locations in different regions of the North Atlantic have been equipped with PIES as part of the NOAC effort, with deployment periods ranging from annual to decadal times (Table 1). Volume transport for the western part of the 47°/48°N section (west of 31°W) have been published by Rhein et al. (2019), transports across the western flank of the MAR by Roessler et al. (2015), updates in McCarthy et al. (2020) and Rhein et al. (2019) Distinguished time series of volume transport from the eastern basin are not yet available. In order to provide this information, we focus on the region between 31°W (BP12) and 15°W (BP32) for the volume transport calculations, where we have PIES data for the period 2016–2017 (Table 1). Data from all 12 PIES stations (Figure 1) are used to discuss the correlation between PIES measurements of the baroclinic and barotropic contribution to SSH fluctuations with satellite measured SSH, and to compare the inferred transport time series from the eastern basin to those obtained from the western basin and from the MAR region.

The bottom pressure is measured by each PIES once per half an hour, the acoustic travel time τ is measured 12 times per half an hour. Daily mean values for bottom pressure and τ are calculated as described in the Inverted Echo Sounder User Manual by University of Rhode Island (2015). The unknown drift of the pressure sensor is removed following Roessler et al. (2015) and Watts and Kontoyiannis (1990), and only bottom pressure fluctuations are taken into account. Data retrieval either takes place via acoustic telemetry while the instrument remains in the water or after the instrument is recovered. During telemetry, only the daily mean values are transmitted whereas after the recovery of the instrument, the full resolution data set can be downloaded from the instrument's hard disk. Here, we only use the daily mean values. For some PIES positions, the time series exhibits gaps due to technical issues, and not all positions were continuously equipped with an instrument (cf. Table 1).

Table 3
Research Cruises From Which CTD Data are Used to Create the Transfer Function for NAC East PIES

Research vessel	Cruise	Date CTD stations	# Stations	DOI/Reference
Maria S. Merian	MSM53	6 Apr 2016–12 Apr 2016	20	10.2312/cr_msm53
Sarmiento de Gamboa	OVIDE - BOCATS2016	30 Jun 2016–3 Jul 2016	9	10.20350/digitalCSIC/8513, (Perez et al., 2018)
Celtic Explorer	CE17007	15 May 2017–19 May 2017	15	Personal communication (cruise report: https://cchdo.ucsd.edu/data/14809/45CE20170427_do.pdf)
Maria S. Merian	MSM64	6 Jun 2017–11 Jun 2017	13	10.2312/cr_msm64
Maria S. Merian	MSM73	12 Apr 2018–14 Apr 2018	6	10.2312/cr_msm73
Thalassa	OVIDE2018	23 Jun 2018–25 Jun 2018	9	10.17600/18000510, (Lherminier, 2018)

CTD, conductivity-temperature-depth; NAC, North Atlantic Current; PIES, pressure sensor equipped inverted echo sounders.

2.2. Hydrographic Data

Hydrographic data of temperature, salinity and pressure obtained from Argo floats and shipboard conductivity-temperature-depth (CTD) measurements are used to create a transfer function to convert the PIES-derived travel times τ into water column profiles of specific volume anomalies (SVA). This procedure is called Gravest Empirical Mode (GEM) method (Meinen et al., 2004; Meinen & Watts, 1998, 2000; Watts et al., 2001) and will be presented in more detail in the next section. From the reconstructed SVA profiles at each PIES position, baroclinic SSH fluctuations are calculated, and from the difference between two SVA profiles at two PIES positions, transport fluctuations are inferred. For the transfer function, data from several cruises between 2015 and 2018 are used (Tables 2 and 3). All cruises carried out with *RV Maria S. Merian* (2015–2018) followed the same survey line along 47°/48°N. The *RV Celtic Explorer* cruise (2017) was on a similar track in the eastern basin but on a more southern track in the western basin. The *RV Sarmiento de Gamboa* (2016) cruise sampled the OVIDE line, which intersect the 47°/48°N array at about 20°W.

Since the shipboard CTD data are limited in space and basically only stem from spring and early summer of the respective years, they cannot be used to assess any seasonal changes in the surface layers. We have therefore extended the hydrographic data set by including profile data obtained from the international Argo float program. The Argo float measurement generally cover the upper 2,000 m range of the ocean. The measured profiles have been quality-controlled by Birgit Klein from the Federal Maritime and Hydrographic Agency as described in Kieke et al. (2009). Only delayed mode Argo data with a quality flag 1 reaching as deep as at least 1,900 dbar is considered. The Argo data stems from the time period January 2015 to July 2018, which is a compromise between using a sufficiently large data set to create a robust transfer function and avoiding that the function is distorted by profiles representing a possible different hydrographic situation prevailing at another time. Rhein et al. (2019) estimated that transfer functions based on different five years of Argo/CTD data in the time period 1993–2018 could lead to mean transports for the whole time series that differ by ±10%. The region from which the profiles are taken (Figure 3), is chosen by considering topographic constraints and different hydrographic realms (Figure 1).

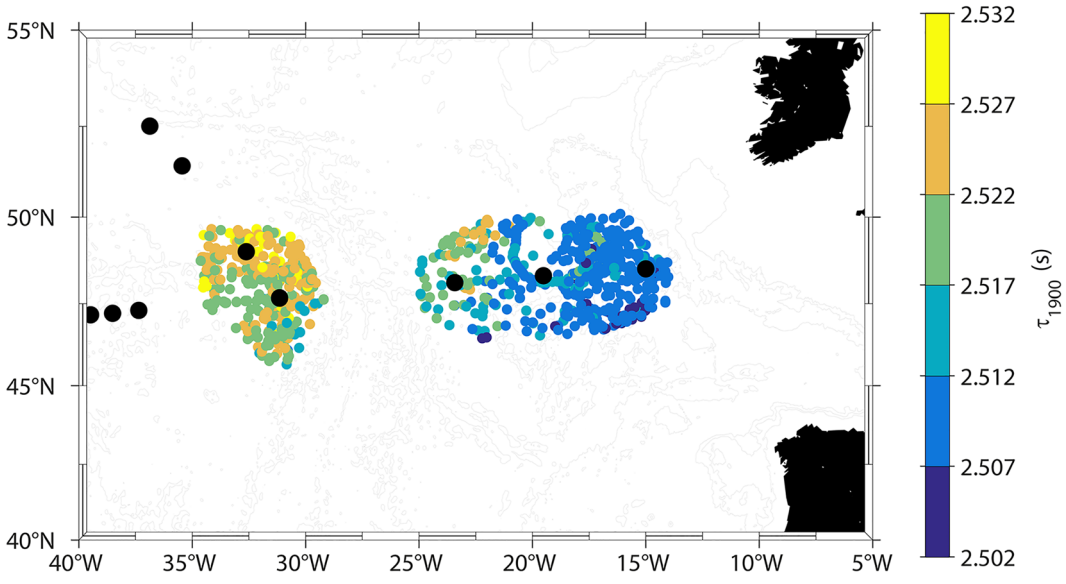

Figure 3. Locations of Argo float and shipboard CTD profiles used to calculate the transfer functions for PIES BP12 in the western basin and the three eastern PIES. Colors denote the acoustic travel time at 1,900 dbar. The black dots show the locations of the PIES. CTD, conductivity-temperature-depth; PIES, pressure sensor equipped inverted echo sounders.

2.3. Satellite Altimetry

In our analysis we use the satellite mapped absolute dynamic topography (MADT), in the following addressed as satellite or altimeter SSH, and satellite absolute geostrophic surface velocities provided by E.U. Copernicus Marine Environment Monitoring Service (product identifier: SEALEVEL_GLO_PHY_L4_REP_OBSERVATIONS_008_047). The satellite data are available on a horizontal grid of 1/4° and span the period 1993–2017 at daily resolution. To classify the different NAC regimes and to analyze the relevance of the baroclinic and barotropic components for the SSH signal in the different regions, the satellite SSH is compared to the baroclinic and barotropic contributions to SSH fluctuations calculated from PIES data. Based on the results of this analysis, the satellite SSH is then used to calculate absolute transport time series for the deployment periods and to extend the baroclinic PIES transport time series backwards in time until 1993. The absolute geostrophic velocities from the same data set are used to analyze the mean surface flow east and west of the MAR crest in the *NAC Central* segment (cf. Figure 14).

3. Methods

3.1. Transfer of PIES Measured Travel Time into Specific Volume Anomaly Profiles

The transfer function (Figure 4) used to convert the PIES travel time measurements into specific volume anomaly profiles is created following Meinen et al. (2004), Meinen and Watts (1998, 2000), Roessler et al. (2015) and Watts et al. (2001). Owing to the different hydrographic conditions in the western and the eastern basins, the transfer function for PIES BP12 located on the western flank of the MAR differs from the one used for the three PIES located in the eastern Atlantic (Figures 3 and 4).

The PIES travel time is transferred into an SVA profile at each PIES site using Argo float and shipboard CTD profiles (Figure 3). All Argo float and shipboard CTD profiles are combined and gridded in 10 dbar intervals down to a maximum depth of 4,500 dbar in case of the three eastern PIES BP32–34 and down to 4,100 dbar for BP12. The two pressure levels 4,500 dbar and 4,100 dbar correspond to the approximate water depths at the PIES positions (Table 1) and are thus chosen as depth limits for the transfer function. For each hydrographic temperature and salinity profile, the acoustic travel time is calculated and corrected for the different latitudes of the Argo float and shipboard CTD data, i.e. the calculated travel time is referenced to a common gravitational acceleration g = 9.8 m/s^2 (Meinen & Watts, 1998; Watts et al., 2001). Then, potential density anomaly and SVA are calculated for each profile. The seasonal signal in τ-space is removed for the upper 250 dbar so that the transfer function can be used for all PIES measurements irrespective of the date at

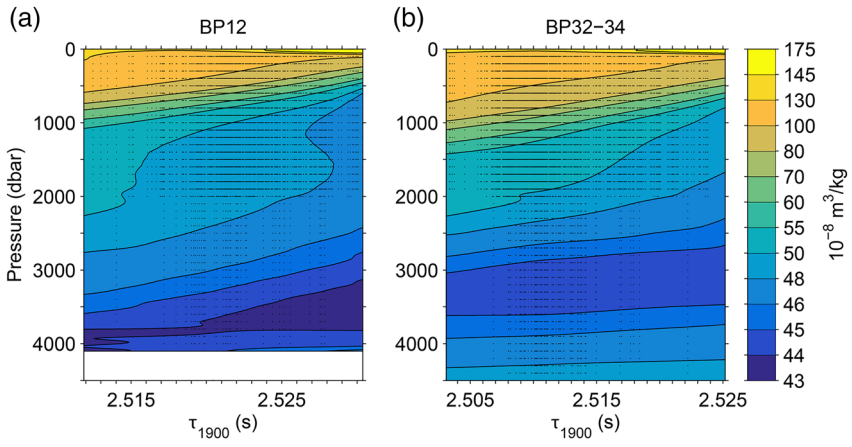

Figure 4. Transfer function between the specific volume anomaly (SVA) calculated from the Argo float and shipboard CTD profiles shown in Figure 3 and the acoustic travel time at the reference pressure level of 1900 dbar for PIES BP12 in the western basin (a) and the PIES BP32–34 in the eastern basin (b) The black dots represent the Argo float and shipboard CTD profiles shown in Figure 3. CTD, conductivity-temperature-depth; PIES, pressure sensor equipped inverted echo sounders.

which the measurement was taken. The profiles are sorted according to τ at 1,900 dbar and cubic smoothing splines are applied horizontally at each pressure level over all τ values. In τ ranges where no deep reaching shipboard CTD data are available, the data set is vertically extrapolated and afterward vertical splines are applied over the whole depth range. Furthermore, a cubic smoothing spline is applied between 1,600 dbar and 2,400 dbar to smooth the transition to depth below 2,000 dbar where considerably fewer measurements are available due to the lack of Argo data.

As the Argo float and shipboard CTD profiles, the acoustic travel time measured by the PIES is also corrected for different latitudes by referencing to g = 9.8 m/s^2. To use the transfer function to convert PIES measurements into water column profiles, it is necessary to reference the travel time measurements onto a common reference pressure level (1,900 dbar). The pressure level of 1,900 dbar is chosen as common reference because each profile used to create the transfer function reaches down to at least this limit. For referencing the travel time measurement onto 1,900 dbar, two steps are necessary. First, CTD data at the PIES positions from the deployment and recovery cruises are used to convert the PIES measured τ into a τ_{4500} (eastern PIES BP32–34) and τ_{4100} (BP12), i.e. the travel time relative to 4,500 dbar and 4,100 dbar, which corresponds to the respective pressure limits of the two transfer functions. This step is necessary because the PIES positions is not exactly at depths of 4,500 dbar or 4,100 dbar. In a next step, the converted τ values are referenced to a common τ_{1900} at 1900 dbar with the following equation from Meinen & Watts (1998, Equation B1):

$$\tau_{P1} = A \times \tau_{P2} + B. \tag{1}$$

In order to determine the coefficients A and B of Equation 1, all the deep reaching CTD data included in the transfer function have been used. The converted τ values are corrected for seasonality in τ-space, and with the help of the transfer function, time series of SVA profiles are reconstructed from the PIES data.

The barotropic contribution to the SSH fluctuation η'_{bt} is calculated as shown in Equation 2 from the bottom pressure fluctuations p'_{PIES}, the density of the water at the sea floor ρ_{bottom} (obtained from the reconstructed profiles) and the gravitational acceleration at the PIES position g (λ, H) depending on latitude λ and the instrument depth H (Teague et al., 1995). η'_{bt} is converted into the barotropic contribution to the travel time τ_{bt} using the sound speed in water c_{sound} calculated with the Del Grosso equation (Del Grosso, 1974) from the reconstructed temperature and salinity water column profiles (Equation 3). τ_{bt} is then removed from the measured τ_{PIES} (Equation 4) to get the baroclinic contribution to τ. The baroclinic contribution τ_{bc} to the measured travel time τ_{PIES} is then used for reconstructing new time series of water column profiles as described before. In a last step, a seasonal model is added to the profiles. It is calculated from the residuals of the measured profiles and the transfer function (Roessler et al., 2015).

$$\eta'_{bt} = \frac{p'_{PIES}}{\varrho_{\mathrm{bottom}} \cdot g\left(\lambda, H\right)} \tag{2}$$

$$\tau_{bt} = 2\frac{\eta'_{bt}}{c_{\mathrm{Sound}}} \tag{3}$$

$$\tau_{bc} = \tau_{pies} - \tau_{bt} \tag{4}$$

3.1.1. Quality Control of GEM Method

To assess the goodness of the transfer function obtained from the GEM method, several quality control measures are performed following Roessler et al. (2015). The first step is to ensure an unambiguous relation between the travel time and water column profiles. For this, the geopotential anomaly (GPA) integrated between 250 dbar and 1,900 dbar plotted against the travel time for 1,900 dbar is explored (Figure 5).

The profiles exhibit a linearly decreasing relation between the integrated GPA and the travel time at 1,900 dbar. This is an indicator for an unambiguous relation between the water column profiles at the respective locations in general and the travel time. The acoustic travel times <2.51 s show larger deviations from the linear correlation in the eastern Atlantic (Figure 5b). This is presumably caused by the presence of the relatively warm and saline Mediterranean Outflow Water (MOW) at intermediate depths, that is not observed in the western basin. Furthermore, travel times that small are mostly not present in the western

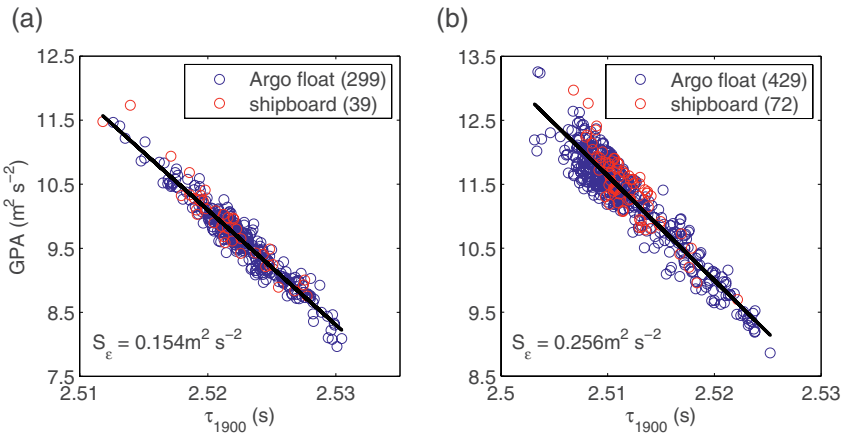

Figure 5. Correlation between acoustic travel time and GPA integrated between 250 dbar and 1,900 dbar for the transfer function for PIES BP12 (a) and the three eastern PIES (b). S_ε denotes the standard error of the fit. Note the different *x*- and *y*-scales. Numbers in brackets indicate number of Argo float and shipboard CTD profiles. CTD, conductivity-temperature-depth; GPA, geopotential anomaly; PIES, pressure sensor equipped inverted echo sounders.

basin. Indeed, the deviations between both transfer functions are largest in the depth range of the MOW between about 600 and 900 m depth (Figure 6). Nonetheless, the correlation between travel time and integrated GPA is good enough (goodness of fit expressed by standard error of the fit) to apply the GEM method also in the eastern basin.

In a second step, the reconstructed sections are compared to the measured cruise section from 2016 (Figures 7 and 8). To do this, the transfer function is calculated without using the hydrographic data from this particular cruise. Even though small-scale features cannot be resolved with the GEM technique due to the necessary smoothing and filtering of the data, the general features of the measured and the reconstructed section look quite similar. Overall, the differences are small compared to the signal itself, which justifies the use of the GEM method and the choice of the Argo and chipboard CTD data shown in Figure 3. Both transfer functions can be used to reconstruct the observed SVA between the two GEMs regimes (Figure 8), i.e. the region which was kept gray in Figure 7, the deviations between observations and reconstructions are not larger than for the regions for which the GEMs were calculated.

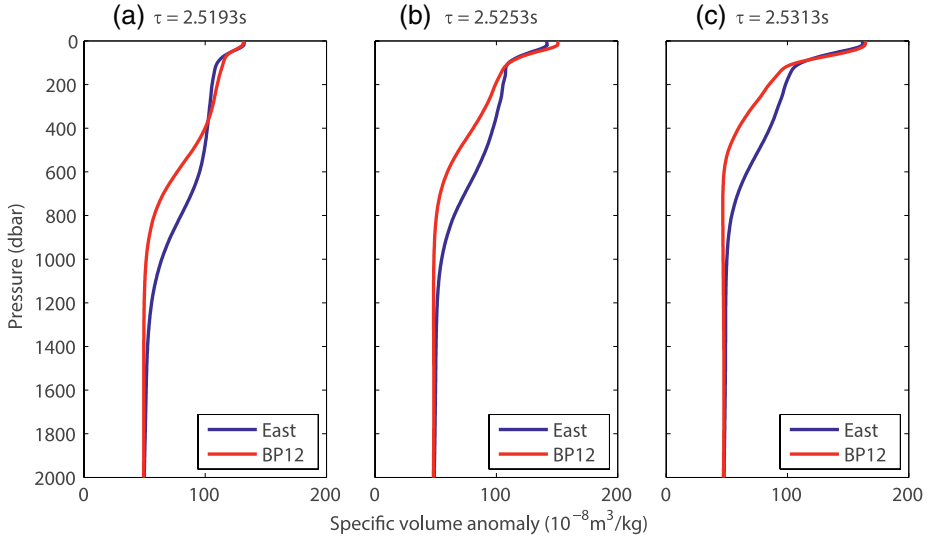

Figure 6. Specific volume anomaly profiles for different acoustic travel times (listed on top) reconstructed from the transfer function for BP12 (red) and for the three eastern basin PIES BP32–34 (blue). PIES, pressure sensor equipped inverted echo sounders.

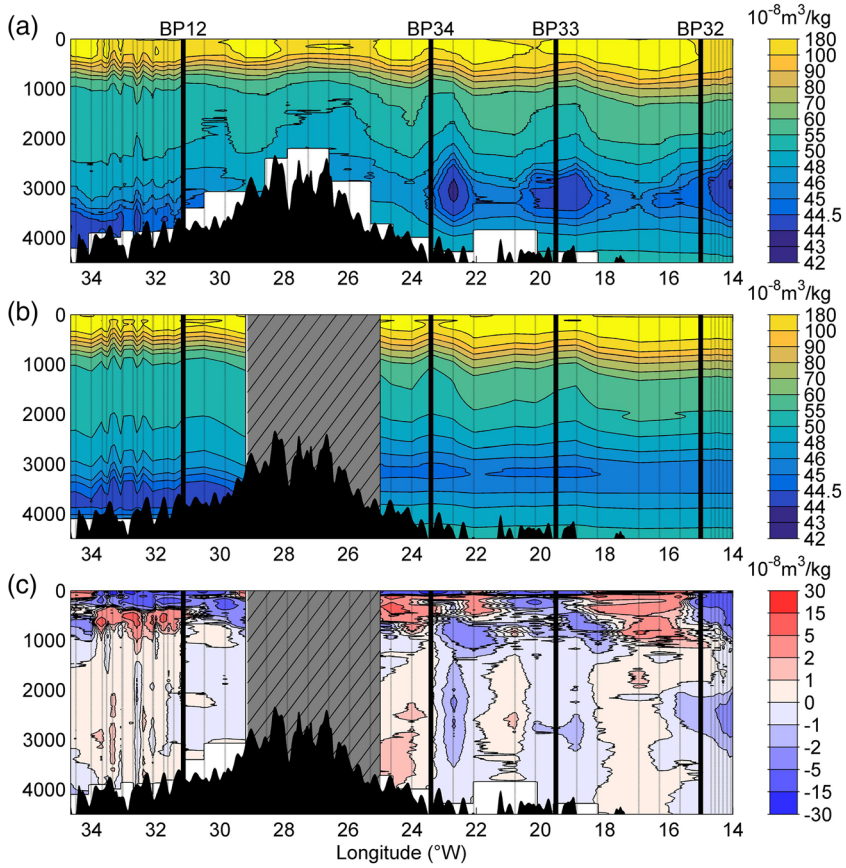

Figure 7. Specific volume anomaly (SVA) from (a) CTD measurements from cruise MSM53 in 2016, (b) SVA based on the GEM reconstructed CTD profiles of this cruise, and (c) the difference between the CTD and GEM reconstructed section. Dashed lines indicate CTD stations, solid thick lines indicate PIES positions. The hatched gray area indicates the transition region between the transfer function for PIES BP12 west of the MAR and the PIES BP32–34 east of the MAR (cf. Figures 3 and 8). CTD, conductivity-temperature-depth; GEM, Gravest Empirical Mode; MAR, Mid-Atlantic Ridge; PIES, pressure sensor equipped inverted echo sounders.

3.2. Barotropic and Baroclinic Sea Surface Height Fluctuations

In order to analyze the different study regions in terms of baroclinic and barotropic contributions to the SSH fluctuations and to reveal different NAC regimes, the correlation between PIES inferred SSH fluctuations and satellite measured SSH is discussed. The barotropic (bt) contribution to PIES inferred SSH fluctuations η'_{bt} is calculated following Equation 2. The baroclinic (bc) contribution η'_{bc} is determined from τ_{bc} which was corrected for the barotropic component (Equation 4) by calculating the GPA as an integral over the reconstructed SVA (Hallock, 1987; He et al., 1998):

$$\mathrm{GPA} = \int_0^p \mathrm{SVA}\,dp, \tag{5}$$

with p being the pressure at the PIES position. With $\mathrm{GPA} = \overline{\mathrm{GPA}} + \mathrm{GPA}'$ the baroclinic contribution to the SSH variability η'_{bc} becomes:

$$\eta'_{bc} = \frac{\mathrm{GPA}'}{g(\lambda, H)}, \tag{6}$$

with $g\,(\lambda, H)$ as the gravitational acceleration at the PIES position.

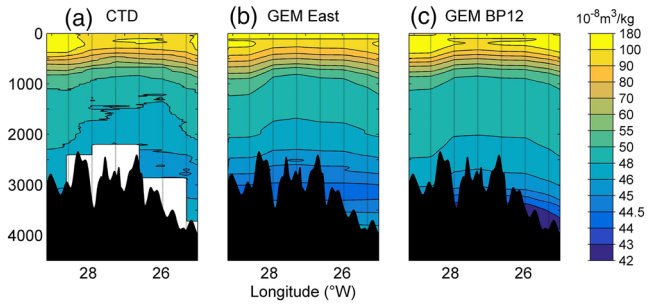

Figure 8. Transition area between region of GEM for BP12 and GEM for eastern PIES. (a) SVA from CTD measurements, (b) SVA reconstructed from GEM for eastern PIES BP32–34, (c) SVA reconstructed from GEM for BP12. CTD, conductivity-temperature-depth; GEM, Gravest Empirical Mode; PIES, pressure sensor equipped inverted echo sounders.

3.3. Barotropic and Baroclinic Transport Fluctuations

In order to complement the meridional transport calculations at the NOAC array, data from the PIES BP12 (west of the MAR) and the three eastern PIES BP32–34 is used. From respectively two PIES measurements a barotropic and baroclinic contribution to the velocity profile and thus the transport between these two PIES is inferred. The barotropic contribution to the velocity profile v'_{bt} is calculated from the bottom pressure fluctuations of two PIES, the mean density $\overline{\rho}$, calculated from the reconstructed water column profiles at the PIES positions, the mean Coriolis parameter of the two locations and the distance between the two PIES:

$$v'_{bt} = \frac{p'_{\mathrm{PIES}}}{\overline{\rho}.f(\lambda).distance}. \tag{7}$$

From the reconstructed SVA water column profiles at two PIES positions, the geostrophic velocity relative to a reference level at 4,500 dbar (transport between BP32 and BP33 and between BP33 and BP34) or 4,100 dbar (transport between BP12 and BP34) is calculated. The obtained velocity profiles are defined as the baroclinic contribution. The barotropic velocity component is added and both together are defined as the total relative PIES-derived velocity. In order to calculate the transport between two PIES, the velocity profile has to be multiplied with the area of the cross section spanned by the two PIES. Obviously, this area is not exactly rectangular, especially not in the case of the cross section between BP12 and BP34 which includes the MAR. To account for the topography in the calculation of the size of the cross section, we use the ETOPO1 topography data set (Amante & Eakins, 2009). The velocity profiles are extrapolated down to the sea floor in cases where the seafloor is below the GEM pressure limit of 4,500 dbar/4,100 dbar or cut off at the respective pressure level in cases where the sea floor is above the GEM pressure limit. From these extrapolated or truncated velocity profiles, which are multiplied with the area of the cross section, the total relative PIES-derived transport between two PIES is calculated. However, since the barotropic contribution is only a transport fluctuation and the baroclinic contribution is calculated to a reference level of no motion, without further known reference level (cf. Section 3.4), the resulting time series represents thus only a relative transport.

3.4. Absolute PIES Transport Time Series

For all transport sections, a high correlation between the geostrophic surface velocities calculated from the satellite SSH and the baroclinic PIES transports is found (all correlation coefficients are above 0.85). The PIES-derived barotropic transport fluctuation varies independently from the baroclinic transport and also exhibits a smaller variability compared to the baroclinic signal. It is thus not imprinted well on the altimeter signal and for all transport sections the correlation between the satellite geostrophic surface velocities and the barotropic PIES transports is not significant at the 95% confidence limit. These findings are very similar to and supported by the results of the analysis of the different NAC regimes in terms of SSH fluctuations presented and discussed in section 4.1. We use the high correlation between the satellite record and the PIES data to obtain absolute baroclinic PIES-derived transport time series following Rhein et al. (2019). We reference the PIES-derived baroclinic velocities which are relative to an assumed reference level to the geostrophic velocities calculated from the satellite SSH to obtain absolute PIES-derived baroclinic velocity profiles and consequently transport time series. In a last step, the PIES-derived barotropic transport fluctuations are added to the absolute PIES-derived baroclinic transport time series to obtain the total PIES-derived daily transport for the period 2016 to 2017.

3.5. Transport Time Series Extended by Altimetry

To extend the transport time series back to 1993 the absolute baroclinic transports are regressed on the altimeter surface velocity field. In contrast to the flow field in the western basin west of 37°W (see also Figures 9 and 10), the barotropic part of the flow in the four PIES considered here is not correlated well with altimetry as stated above. Consequently, we obtain a daily baroclinic transport time series for the period 1993–2017 with the barotropic component representing an uncertainty in the interpretation of the altimeter signal as proxy for the transport.

4. Results and Discussion

In the following, we introduce the results from our correlation analysis and present and discuss the first PIES-derived transport time series for the eastern basin across 47°/48°N. These are extended into decadal time series by means of satellite data and are put into relation to corresponding time series from the western basin and the MAR region (cf. Figure 1).

4.1. Correlation Between PIES and Altimeter-Derived SSH Data

Figure 9 shows a comparison of selected PIES representing the western, central and eastern NAC regimes regarding baroclinic and barotropic contributions to the SSH fluctuation. The time series are shortened to show the same time period in each panel. Figure 10 summarizes the correlation coefficients for the comparison of baroclinic and barotropic contributions to the PIES-derived SSH fluctuation with the satellite-derived SSH for each PIES site. The correlation between the SSH calculated from the PIES data and the altimeter measurements reveal different dynamical regimes. In the western Atlantic west of 37°W, the barotropic as well as the baroclinic contribution to the PIES-derived SSH signal is highly correlated with the altimeter signal, while at the MAR and in the eastern Atlantic, the correlation of SSH with the barotropic signal is for most cases not significant and thus negligible when considering the total signal (Figure 10). This reflects two dynamical regimes: West of 37°W, the flow has strong barotropic signals (Figure 9a) with top-bottom averaged mean velocities of the order of tenths of cm/s (Rhein et al., 2019), while at the MAR (Roessler et al., 2015) and in the eastern Atlantic the variability of the barotropic signals is smaller with a very weak imprint on the SSH (Figures 9b–9d).

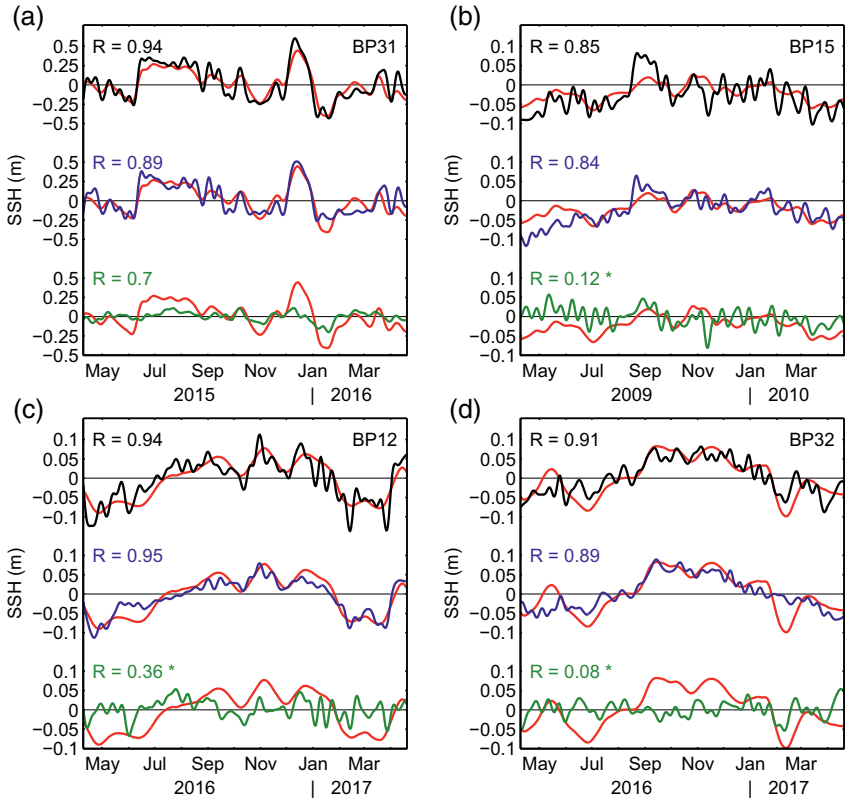

Figure 9. Comparison of time series of barotropic (green), baroclinic (blue) and barotropic + baroclinic (black) SSH fluctuations to satellite SSH fluctuations (red) from (a) PIES BP31 (western endpoint of 47°/48°N-array), (b) PIES BP15 (northern endpoint of MAR array), (c) PIES BP12 (located at the midpoint connecting the MAR- and 47°/48°N-array), and (d) PIES BP32 (eastern endpoint of 47°/48°N-array). For each comparison, the corresponding correlation coefficient R is given. The asterisk marks non-significant correlations at the 95% confidence limit ($p > 0.05$). Note the different years on the x-axes and different scales on the y-axes on each figure. To compare time series of the same length and times of the year, the time series were shortened. Correlation coefficients of the unshortened time series are shown in Figure 10. MAR, Mid-Atlantic Ridge; PIES, pressure sensor equipped inverted echo sounders; SSH, sea surface height.

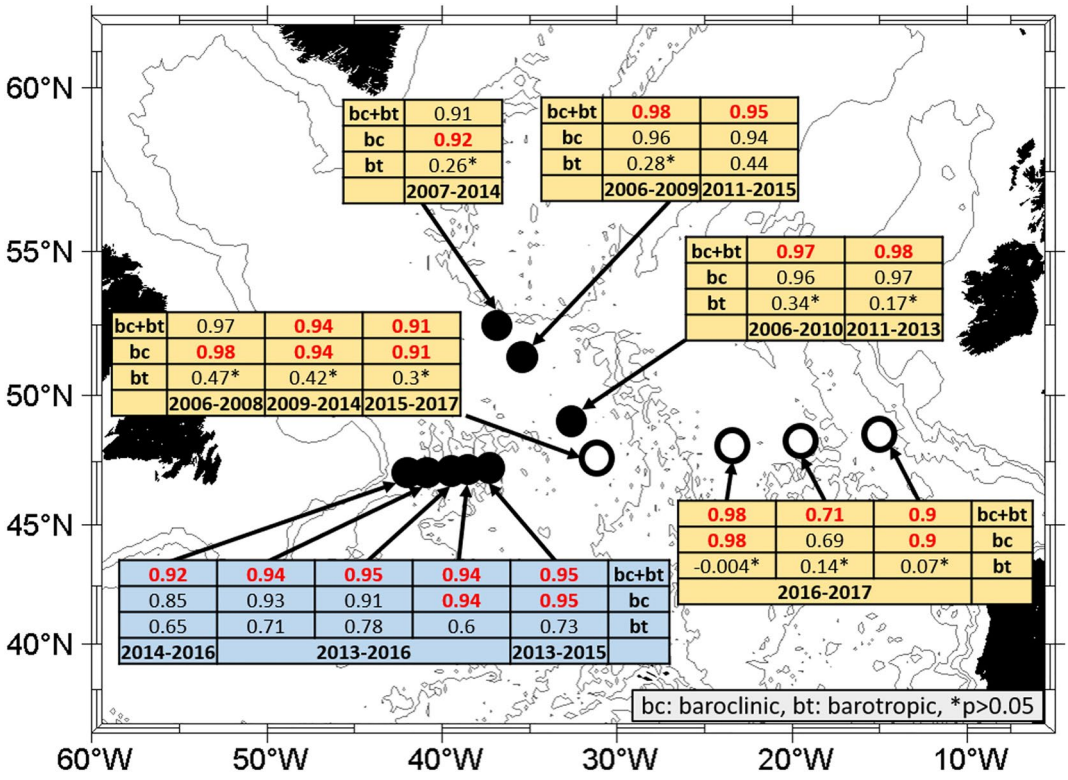

Figure 10. Correlation between the PIES-derived barotropic (bt), baroclinic (bc) and baroclinic + barotropic (bc + bt) contribution to SSH variability and satellite altimetry at the PIES positions. Numbers denote the correlation coefficient with the highest correlation marked in bold red. *P*-values >0.05 indicate that the correlation is not significant at the 95% confidence limit. Table colors indicate the different dynamic regimes: In the western basin (blue) the barotropic PIES signal is imprinted well on the altimeter SSH signal whereas in the eastern basin and the MAR region (yellow), only the baroclinic PIES signal is strongly correlated with the altimeter signal. The correlation is calculated under consideration of the decorrelation time for each 10-days low pass filtered time series. The decorrelation time scale is calculated as twice the integral of the lagged autocorrelation function (Bayley & Hammersley, 1946; Garrett & Petrie, 1981; Rhein et al., 2019; Roessler et al., 2015). For the altimeter-derived SSH fluctuation, the decorrelation time is in the range of 16–109 days, for the barotropic PIES-derived SSH fluctuation, it is in the range of 7–35 days, for the baroclinic PIES-derived SSH fluctuation, it is in the range of 19–86 days, and for the sum of the baroclinic and barotropic PIES-derived SSH fluctuation, it is in the range of 15–82 days. MAR, Mid-Atlantic Ridge; PIES, pressure sensor equipped inverted echo sounders; SSH, sea surface height.

4.2. Transports

In the following we present the PIES-derived transport timeseries from 2016 to 2017, including the total top-to-bottom transport (Figure 11) as well as the transport in upper and lower layers (Figure 12). We furthermore present the reconstructed long-term timeseries (1993–2017) which were obtained using satellite altimetry data (Figure 13). Table 3 summarizes the mean PIES-derived transports for the different NAC

Table 4
Mean Values, Standard Error of the Mean, Standard Deviation, Effective Degrees of Freedom, and Decorrelation Time Scale for the PIES Transport Time Series, May 2016–June 2017 (cf. Figure 11)

	NAC Central	NAC East 1	NAC East 2	Sum
Mean (Sv)	11.1	−1.4	2.5	12.2
Standard error of the mean (Sv)	1.7	1.8	1.7	1.4
Standard deviation (Sv)	8.6	8.6	7.9	8.7
Degrees of freedom	26	24	23	39
Decorrelation time scale (days)	16	17	18	11

Note. The standard error of the mean is used as a measure of uncertainty for the calculated mean transports.
NAC, North Atlantic Current; PIES, pressure sensor equipped inverted echo sounders.

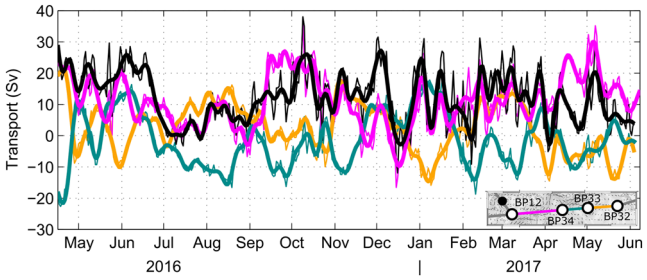

Figure 11. Total (absolute baroclinic + barotropic) PIES derived transport as daily values (thin lines) and 10-day low pass filtered (thick lines) in the period April 2016–June 2017. Ekman transport not included. Positive values: northward transport, negative values: southward transport. NAC Central segment: magenta, NAC East 1 segment: green, NAC East 2 segment: yellow, sum of all three segments: black. For mean transports cf. Table 4. NAC, North Atlantic Current; PIES, pressure sensor equipped inverted echo sounders.

segments obtained in the measurement period April 2016–June 2017, Table 4 summarizes the mean transports for the extended time series.

For the measurement period 2016–2017, we find the largest mean northward transport (+11.1 Sv ± 1.7 Sv) in the *NAC Central* segment, a smaller mean southward transport in the *NAC East 1* part (−1.4 Sv ± 1.8 Sv) and a smaller mean northward flow in the easternmost segment *NAC East 2* (+2.5 Sv ± 1.7 Sv). Even if we scale the transports with the distance between the PIES, the transport in the *NAC Central* segment is more than twice as high as in the *NAC East 2* part and almost four times larger than the *NAC East 1* segment. The maximum transport in the central segment is of the order of 30 Sv and the maximum transport lasting longer than a month of 25 Sv (Figure 11). To what extent these 14 months of data are representative of the mean flow and the observed variability will be further explored when addressing the reconstructed decadal time series (Figure 13).

The ADCP velocity section (Figure 2) suggests that east of the main NAC branch, recirculation and southward in the western basin, the flow at depth is sometimes opposite to the flow in the upper layers. In order to

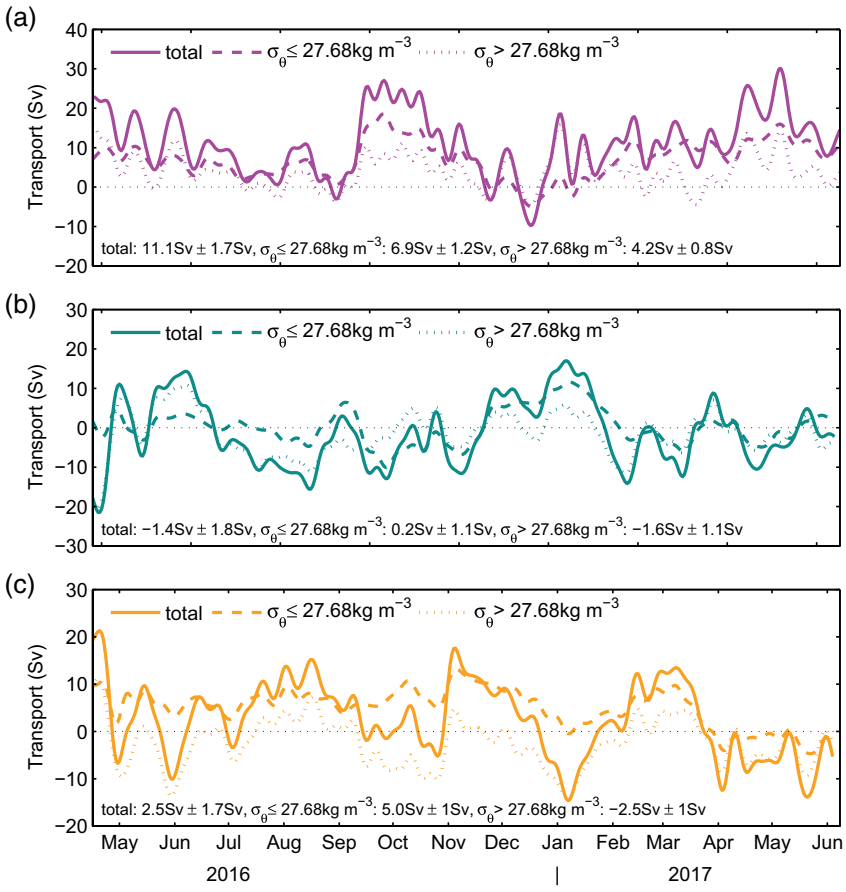

Figure 12. Total top-to-bottom transport (solid line) and transport below (dotted line) and above (dashed line) the 27.68 kg/m³ potential density isoline for the segments NAC Central (a), NAC East 1 (b) and NAC East 2 (c). Transports are 10-day low pass filtered. Numbers represent mean transports and standard errors of the mean for each transport section and are given in each panel for the total transport and the transport below and above the chosen isoline. Positive values: northward transport, negative values: southward transport. The chosen isoline for separating between upper and lower transports corresponds to an average pressure level of 1,030 dbar. NAC, North Atlantic Current.

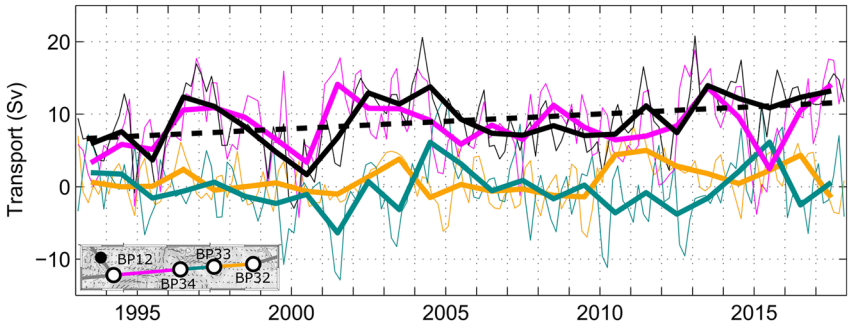

Figure 13. Absolute baroclinic PIES transport expanded with satellite altimetry (1993–2017). Solid thin lines: bi-monthly means, solid thick lines: annual means, dashed line: decadal trend for the sum of all segments. Colors as in Figure 11. The Ekman transport is not included. For mean transports cf. Table 5. Significant decadal trend for all segments together +2 Sv ± 1.5 Sv ($p = 0.01$). PIES, pressure sensor equipped inverted echo sounders.

address this difference, we therefore calculated the flow at depth and in the upper layers separately and in addition to the total top-to-bottom transport (Figure 12). The isopycnal $\sigma_\Theta = 27.68$ kg/m³ which corresponds in average to a pressure level of 1,030 dbar (averaged over all three sections, *NAC Central*, *NAC East 1* and *NAC East 2*, and the time period 2016/2017) was chosen as a separation between the flow at depth and in the upper layers. This isopycnal represents the upper limit of Labrador Sea Water, the lightest water component of North Atlantic Deep Water. The net northward transport in the upper layer of all three segments (12.1 Sv) is as high as the net top-to-bottom transport in that region (12.2 Sv). The biggest difference between the upper and lower layer is in the *NAC East 2* segment, where the northward transport in the upper layer (5 Sv) is almost as high as in the *NAC Central* segment (6.9 Sv). In the deep layer, however, the *NAC East 2* segment transport is southward (−2.5 Sv), while in the *NAC Central* segment it is northward (4.2 Sv). In the *NAC Central* segment, the transport separation between the upper layer (62%) and deep layer is comparable to the transports across the MAR (upper layer transport equals 61% of the total transport) as reported by Roessler et al., (2015). Due to the high variability of the flow field, however, we cannot infer the amount of subtropical water from this because, in contrast to Roessler et al. (2015), we cannot clearly differentiate between subtropical and recirculated water. Furthermore, because of the relatively short mooring period for the PIES in the eastern basin, we refrain from extrapolating this result to the time period 1993–2017.

Over the time period from 1993 to 2017 (Figure 13), the mean pattern is not so much different compared to the short PIES-derived time series from 2016 to 2017 (Figure 11). The annual mean transport obtained from the decadal time series (Table 5) is northward (overall mean: +9.1 Sv ± 0.8 Sv) and dominated by the almost permanent northward flow in the *NAC Central* segment (overall mean: +8.5 Sv ± 0.6 Sv). This agrees with Stendardo et al. (2020) who find branches splitting from the NAC south of the NOAC array and transporting water directly into the eastern subpolar North Atlantic without following the pronounced NAC branch in the western basin and Kwon and Riser (2005) who use profiling floats to monitor the circulation in the

Table 5
Mean Values, Standard Error of the Mean, Standard Deviation, Degrees of Freedom, and Decorrelation Time Scale for the PIES- and Altimeter-Based Transport Time Series 1993–2017 (Figure 13)

	NAC Central	NAC East 1	NAC East 2	Sum
Mean (Sv)	8.5	−0.3	0.9	9.1
Standard error of the mean (Sv)	0.6	0.6	0.4	0.8
Standard deviation (Sv)	5.5	5.1	3.5	4.8
Degrees of freedom	75	76	68	36
Decorrelation time scale (days)	122	120	133	256

Note. The standard error of the mean is used as a measure of uncertainty for the calculated mean transports. NAC, North Atlantic Current; PIES, pressure sensor equipped inverted echo sounders.

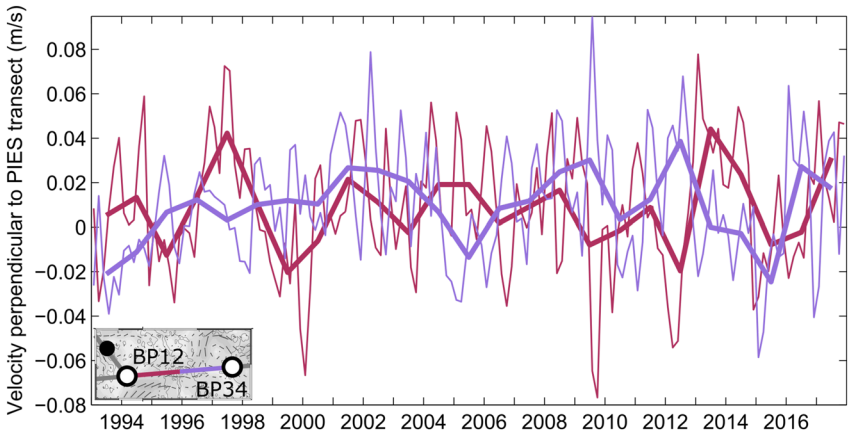

Figure 14. Bi-monthly (thin lines) and annual mean (thick lines) altimeter-derived surface velocities (absolute geostrophic velocities) perpendicular to the NAC Central segment for the period 1993–2017. Data are averaged between PIES BP12 and the MAR crest (red) and the MAR crest and BP 34 (purple). Mid of transect (27°17.06'W) is defined as separation. MAR, Mid-Atlantic Ridge; NAC, North Atlantic Current; PIES, pressure sensor equipped inverted echo sounders.

North Atlantic and observe a float entering the subpolar eastern North Atlantic after crossing the 47°/48°N transect east of the MAR.

The eastern segments *NAC East 1* and *NAC East 2* generally show a near zero flow with tendency to a southward flow for the *NAC East 1* segment (overall mean: −0.3 Sv ± 0.6 Sv) and a tendency to a northward flow for the *NAC East 2* segment (overall mean: +0.9 Sv ± 0.4 Sv). The exceptions are 2005 for the *NAC East 1* segment (+7 Sv) and 2011 (+6 Sv) for the *NAC East 2* segment. The former is correlated with a relatively small transport in the central segment, indicating an eastward shift of the flow regime and a meandering and shifts of the currents. A similar pattern was also observed in 2015, when the northward transport in the *NAC Central* segment decreased from +16 Sv to +2 Sv from 2013 to 2015 and the southward flow in the *NAC East 1* segment of −4 Sv in 2013 turned into a northward transport of +3 Sv in 2015.

In Figure 14, the satellite-derived geostrophic velocities across the *NAC Central* transect are shown, separated between the region west and east of the crest of the MAR. This further analysis of satellite geostrophic velocities could not reveal a more pronounced pathway within the *NAC Central* segment at the eastern or western flank of the MAR (Figure 14). Instead we assume that a meandering of the currents within this segment takes place. What we can see, however (Figure 15), is that, while still being visible in times of higher northward transport across the *NAC Central* segment, during times of lower northward transport, a more pronounced branch detaching from the NAC main branch at about 43°N is found, flowing northeastward, and crossing the MAR south of the 47°/48°N line. In times of lower northward transport in the *NAC Central* segment, this branch tends to cross the 47°/48°N line further east than in times of higher northward transport. This supports our assumption that a meandering of currents and, in times of lower transports across the *NAC Central* segment, even eastward shifts into the neighboring segments occur. It also supports our interpretation of the northward transport in the *NAC Central* segment as another pathway of subtropical water into the eastern subpolar North Atlantic, even though it is also evident from the figure that not all water crossing the transect in northward direction is of subtropical origin but also is recirculating water.

West of 31°W, including the main part of the Newfoundland shelf region and the Ekman transport, the mean meridional top-to-bottom transport was reported to be −9.8 Sv during 1993–2018 (Rhein et al., 2019). The mean Ekman transport across the whole transect from BP12 to BP32 was found to be −1 Sv in 2016–2017 and –1.5 Sv in 1993–2017 (calculated from NCEP/NCAR reanalysis data, Kalnay et al., 1996). The mean top-to-bottom transports in interior eastern Atlantic in 1993–2017 (including the segments *NAC Central*, *NAC East 1* and *NAC East 2* and Ekman transport) sum up to +7.6 Sv and thus seem to compensate about 78% of the flow in the western basin. Assuming mass balance across the whole section, a northward transport of 2.2 Sv is left for the eastern boundary and the eastern shelf.

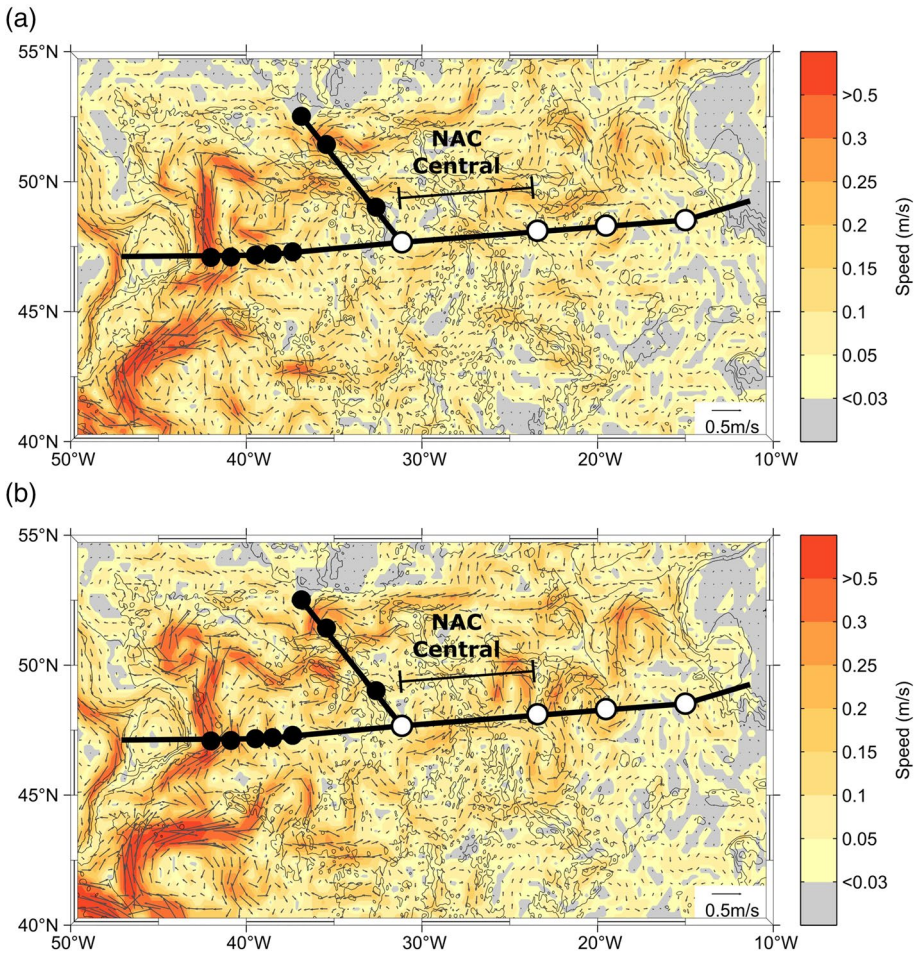

Figure 15. Mean geostrophic velocities in 2016/2017 averaged over time periods with a (a) larger northward and (b) smaller transport across the NAC Central segment. A larger northward transport is defined as transport larger than the mean PIES transport across the NAC Central segment (11.1 Sv) plus the standard deviation (8.6 Sv) and smaller transport is defined as transport below the mean PIES transport minus the standard deviation (cf. Figure 11 and Table 4). Colors and arrows as in Figure 1a, black and white circles represent PIES positions, the lines show the location of the NOAC array. MAR, Mid-Atlantic Ridge; NAC, North Atlantic Current; PIES, pressure sensor equipped inverted echo sounders.

Table 6
Long-Term Trends (Sv/Decade) and Mean Transports 1993–2017 (Sv)

Segment	Trends Sv/ decade	Mean transports (Sv)
NAC Central	+1.2 ± 1.4	+8.5 ± 0.6
NAC East 1	+0.1 ± 1.3	−0.3 ± 0.6
NAC East 2	+0.7 ± 0.8	+0.9 ± 0.4
NAC Central + East 1 + East 2	**+2.0 ± 1.5**	**+9.1 ± 0.8**
NAC West[a]	**−6.0 ± 5.7**	**+19.3 ± 3.3**
NAC West + boundary current [a]	**−7.1 ± 3.9**	**−3.8 ± 2.6**

Note. The transport errors are summarized in Table A2 and standard errors of the mean in Tables 4 and 5. Bold: trend significant with $p < 0.05$. NAC, North Atlantic Current.
[a] from Rhein et al., (2019), time series 1993–2018.

This number is in the range of former transport estimates of the eastern boundary current between 1.5 Sv and 4.7 Sv (Ellett & Martin, 1973; Huthnance, 1986; van Aken & Becker, 1996).

Roessler et al. (2015) analyzed the inflow from the western into the eastern subpolar basin between 47°40'N and 53°N across the MAR. The updated mean (1993–2018) transport of 32.3 Sv (McCarthy et al., 2020) and the northward flow into the eastern Atlantic across 47°/48°N (9.1 Sv) sum up to 41.4 Sv, with the latter contributing 22% to the total flow. At the OVIDE line further northeast, repeat ship-based hydrographic and velocity measurements (Mercier et al., 2015) resulted in a total NAC related transport across that line of 41.8 Sv, i.e. significantly larger than the MAR inflow reported by Roessler et al. (2015). Therefore, Daniault et al. (2016) postulated that part of the NAC enters the subpolar gyre directly in the eastern basin without the detour through the Newfoundland basin, while Rhein et al. (2011) and Roessler et al. (2015) assumed that this southern-

most branch of the NAC remains in the subtropical region. To make the NAC transport across the MAR and the OVIDE line compatible, a northward flow across 47°/48°N of the order of 9.5 Sv is needed. This number is comparable to the mean observed inflow through the *NAC Central* segment of 8.5 Sv ± 0.6 Sv or to the mean inflow over the central and eastern segments of 9.1 Sv ± 0.8 Sv found in our study (Table 5).

4.3. Long-Term Trends

For the interior western basin and the period 1993–2018, Rhein et al., (2019) found a negative decadal transport trend of −6.0 Sv ± 5.7 Sv (−7.1 Sv ± 3.9 Sv when the western boundary current is included), dominated by the trend in the region between 37°W and 31°W (−4.4 Sv ± 3.7 Sv). The trends are related to the significant positive SSH trends at the western boundary with no or negligible trends in the interior (Rhein et al., 2019, their Figure 11). Following the ocean heat content trends from Häkkinen et al. (2016), Rhein et al. (2019) attributed the positive SSH trends at the western and eastern boundary with none or small (mostly insignificant) trends in the interior to be responsible for the long-term transport trends in the western basin and argued for a positive trend in the eastern basin. The decadal transport trend in the eastern basin found in our study is indeed positive and significant (+2 Sv ± 1.5 Sv), compensating about 30% of the

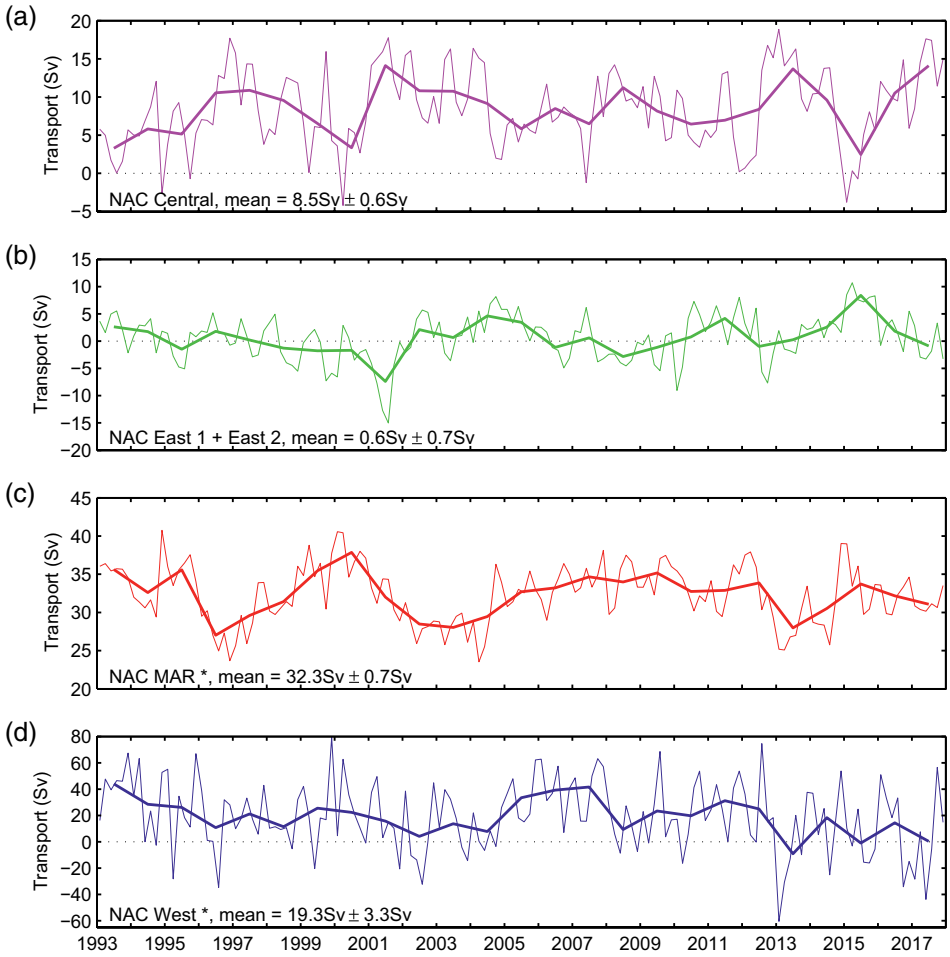

Figure 16. Bi-monthly (thin) and annual mean (bold) transport time series (Sv) at the NOAC site (Ekman transport not included) between 1993 and 2017, (a) the NAC Central segment between 31°W and 23°W, (b) the sum of the eastern segments (NAC East 1 and NAC East 2) between 23°W and 15°W (c) NAC MAR: across Mid-Atlantic Ridge between 47°40'N and 53°N (update from Roessler et al., 2015) and (d) NAC West: meridional flow in the interior western basin between 42°W and 31°W (from Rhein et al., 2019). Numbers indicate mean transport and standard error of the mean for the respective transport section. * values from Rhein et al. (2019), note: time series are only shown until end of 2017 but in the calculation of the mean values and standard errors also data from the year 2018 are used. NAC, North Atlantic Current.

Table 7
Correlation Coefficients Between Annual Mean Flow Components at 47°/48°N and Across the MAR (Figure 16)

Transport 1	Transport 2	Correlation coefficient R
NAC Central	NAC East 1 + NAC East 2	**−0.5**
NAC Central	NAC MAR	**−0.6**
NAC Central	NAC West	**−0.5**
NAC East 1 + NAC East 2	NAC MAR	−0.1
NAC East 1 + NAC East 2	NAC West	0.2
NAC Central + NAC East 1 + NAC East 2	NAC MAR	**−0.7**
NAC Central + NAC East 1 + NAC East 2	NAC West	**−0.4**
NAC MAR	NAC West	**0.6**

Note. Bold: Correlation coefficient is significant at the 95% confidence level. NAC MAR: updated transport time series from Roessler et al. (2015), NAC West: from Rhein et al. (2019, their Figure 9b).
MAR, Mid-Atlantic Ridge; NAC, North Atlantic Current.

transport trend found in the western Atlantic. The trend is dominated by the transport in the *NAC Central* segment (Table 6).

One would expect that the long-term positive trend in the transport across 47°/48°N east of 31°W would lead to a slow salinification of the eastern subpolar basin, and this is somewhat inconsistent with the observed freshening in the time period 2012–2016 (Holliday et al., 2020). On the other hand, the strong inter- and multiannual variability of the transport time series might override the trend. For instance, in 2012–2016, the NAC transport across the MAR was lower than average (mean in 2012–2016: 31.6 Sv, mean in the five years before (2007–2011): 33.9 Sv, cf. Figure 16c). Holliday et al. (2020) attributed the freshening to a slowing of the NAC in the western basin - which is confirmed by the lower *NAC West* transports at 47°/48°N (Figure 16d) and across the MAR at that time period (Figure 16c) - and to a higher than normal Arctic freshwater contribution from the western boundary into the eastern basins. Apparently, only a part is compensated by the

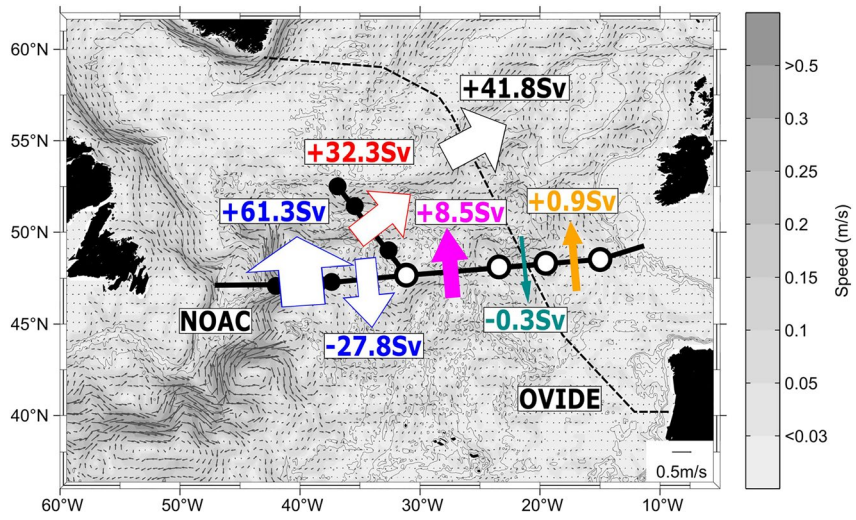

Figure 17. Interior circulation scheme (boundary currents are excluded) at the NOAC array combining results from this paper with results from the western basin (Mertens et al., 2014; Rhein et al., 2019) and the updated transport time series at the MAR, following Roessler et al. (2015), and the OVIDE array (Daniault et al., 2016). In the western basin, the big white arrows show the net northward transport including the NAC and the southward flows east and west of the NAC (61.3 Sv) and the southward flow west of 37°N (−27.8 Sv). At the OVIDE line, the NAC related northeastward transport between 46.14°N and 57.17°N is shown. Arrow widths representing the mean top-to-bottom transports across the sections are not to scale. In the background, the mean geostrophic velocity field is shown (as in Figure 1a). MAR, Mid-Atlantic Ridge; NAC, North Atlantic Current.

anomalous high transport across 47°/48°N east of 31°W. But since our analysis does not include the characteristics of the water masses, we cannot exclude that this branch of the circulation might also be fresher than usual. Another point to consider is the possibility that the main transport in the *NAC Central* segment follows different pathways in 2012–2016. The mean satellite geostrophic velocities across the *NAC Central* transect (Figure 14) show indeed that after 2012 and approximately until 2016, the northward pointing surface velocities in the eastern part indeed decreased and even changed direction from northward to southward.

4.4. Correlation Between Transports Across the MAR and the Meridional Flow in the Western and Eastern Basin

The transport time series discussed here—especially the one representing the *NAC Central* segment—show some patterns that have been also observed in the interior western basin and in the transport across the MAR (Figure 16). There is a positive significant correlation between the interior western basin (*NAC West*) and the MAR transport (+0.6, Table 7). In contrast, the *NAC MAR* transport and *NAC West* transport are both significantly anticorrelated to the flow between 31°W and 15°W (*NAC Central* + *NAC East 1* + *NAC East 2*). In general, a higher northward transport into the interior western basin (*NAC West*) leads to a higher transport across the MAR into the eastern basin, while the northward transport in the eastern interior basin between 31°W and 15°W is lower. The *NAC MAR* transport and northward transport across 47°/48°N between 31°W and 15°W partly compensate each other ($R = -0.7$) leading to a smaller variability for the input of subtropical water into the eastern basin than observed in the individual transport time series. The significance of the correlation of the transport between 31°W and 15°W with the *NAC MAR* transport and with the *NAC West* transport is mainly owed to the *NAC Central* segment, where most of the meridional transport occurs (Figures 13 and 16). The mean annual transport estimates with significant high (anti-)correlations have one common feature: They include 31°W (PIES BP12) as one of their bounds. The variability at the other end points of the transport sections do seem to have a smaller influence on the correlations. That is somewhat surprising, since the variability at the western boundary is much larger than in the interior (Figure 9).

5. Summary and Conclusions

Long-term (1993–2017) transport time series at the boundary (47°/48°N) between the eastern subtropical and subpolar gyre in the eastern North Atlantic were calculated using PIES, Argo float and shipboard CTD data and their relation to the dynamic topography measured with satellite altimetry—a method which was already successfully applied to the western basin of the North Atlantic (Rhein et al., 2019) and to the flow across the MAR in the central subpolar North Atlantic (McCarthy et al., 2020; Roessler et al., 2015). The measurements presented in our study confirmed two pathways into the eastern subpolar basin: the zonal flow across the MAR between 47°40'N and 53°N of 32.3 Sv of which about 60% is of subtropical origin (Roessler et al, 2015; update McCarthy et al., 2020) and a more direct pathway across 47°/48°N coming from the south (Figure 17). The latter contributes with 9.1 Sv ± 0.8 Sv about 22% to the total flow of 41.4 Sv which is compatible to the NAC related transport of 41.8 Sv across the Greenland-Portugal OVIDE line (Daniault et al., 2016; Mercier et al., 2015). While Roessler et al. (2015) assumed that most of the eastward NAC transport is of subtropical origin, in our data, we cannot clearly separate recirculated water from water that followed the direct pathway from the subtropics into the eastern North Atlantic.

In the western basin, Rhein et al. (2019) observe a NAC related northward flow of 105.9 Sv, a southward flow west of 41°W of 29 Sv which includes part of the western boundary current (−14.2 Sv), a southward flow further west with the western boundary current of −23.1 Sv, a recirculation in the Newfoundland Basin of −29.8 Sv, and a southward flow east of 37°W of −27.8 Sv. The western boundary current transport of −23.1 Sv as defined in Rhein et al. (2019) misses the part east of 42°W because it is included in the southward flow west of 41°W. The mean western boundary current transport was reported by Mertens et al. (2014) to be 37.3 Sv. In summary, the northward transport of 61.3 Sv and the southward transport of −27.8 Sv in the interior western basin yield a net northward transport in the interior western basin of 33.5 Sv which is comparable to the updated zonal transport across the MAR found by Roessler et al. (2015).

The roughly 41 Sv entering the eastern subpolar basin are partly transported into the Nordic Seas (8.0 Sv, Østerhus et al., 2019), but the main flow, about 33 Sv (a number comparable to the observations of Daniault et al., 2016), is to the west, north of our study region, and forms the northern branch of the subpolar gyre.

The NOAC array does not support a southward transport across 47°/48°N in the east of 31°W (Daniault et al., 2016), but this is most likely due to the too northward location of the array missing the subtropical pathways.

The pathways into the eastern Atlantic are significantly anticorrelated ($R = -0.7$), i.e. a stronger MAR transport corresponds to a weaker transport from the south and vice versa. The transport in the interior western basin (42°W–31°W) is also significantly anticorrelated with the transport in the eastern basin between 31°W and 23°W ($R = -0.5$). Additionally, both time series exhibit opposite decadal trends, i.e. the observed transport decline in the western basin is partly compensated by an increase of the northward flow east of 31°W. The mean transport imbalance at the 47°/48°N section from Newfoundland to 15°W was found to be −2.2 Sv. This imbalance is most likely compensated by the eastern boundary current system. This is encouraging for the application of the PIES/altimetry method for future AMOC estimates at this latitude once observations of the eastern boundary current system and the shelf region are available.

Appendix A: Uncertainties in the PIES transport time series

In the following, we discuss the different sources for uncertainties in the transport time series. For this, the baroclinic and barotropic transport time series from PIES are treated separately from the long-term transport time series obtained by regression on the altimeter data.

A1 PIES Transports

First, the uncertainty for the time series with daily resolution is calculated followed by the uncertainty for yearly mean values obtained by scaling the daily error with the effective number of independent observations (effective degree of freedom, Bayley & Hammersley, 1946; Garrett & Petrie, 1981; Rhein et al., 2019; Roessler et al., 2015). The effective degree of freedom is given in Table A1, the uncertainties are given in Table A2. The combined uncertainties for the baroclinic time series with daily resolution range from 7.5 Sv to 8.8 Sv, for the annual mean values from 2.6 Sv to 2.9 Sv. The uncertainty in the barotropic time series related to the pressure measurement ranges from 1.2 Sv to 1.7 Sv for the daily values and from 0.03 Sv to 0.06 Sv for the annual mean values.

Uncertainty in the Barotropic PIES Transport Fluctuation Related to the Pressure Measurements

The uncertainty for the individual half-hourly pressure measurement related to the de-drifting routine is less than 0.02 dbar (Watts & Kontoyiannis, 1990). To convert this value into an uncertainty in the barotropic transport fluctuation, it is scaled with the effective degrees of freedom ($n = 48$), for a measurement period of 24 h, since the de-drifted and de-tided statistically independent daily mean values are used in the calculations, and multiplied by $\sqrt{2}$, since data from two PIES are used two calculate the transport for a section. This results in an uncertainty of 1.2 Sv–1.7 Sv for the daily values and for the yearly mean values in an uncertainty of 0.03 Sv–0.06 Sv, scaled with the effective degree of freedom from Table A1.

Baroclinic PIES Transport

The uncertainties in the baroclinic transport are caused by several independent sources. As described in Chidichimo et al., (2014), Meinen et al., (2004) and Roessler et al. (2015), they originate from:

1. uncertainties in the τ measurements caused by
   a. scatter in the measurements due to sea roughness and rain, i.e. the measurement accuracy,
   b. scatter from the linear relation between the Fofonoff potential and τ_{1900} (Figure A1),
   c. calibration of the measured τ into τ1900 via CTD measurements,
   d. removal of the barotropic component in the travel time measurement,
2. uncertainties due to the Argo float and shipboard CTD profiles used to create the GEM look-up table
3. uncertainties due to latitudinal differences between the PIES positions.

To determine uncertainties for the yearly mean transports of the complete PIES measurement record, the daily uncertainty for the measurement accuracy of τ, the scatter from the linear fit (cf. Figure A1), the removal of the barotropic component in τ and the error due to different latitudes are scaled with the effective degrees of freedom. The uncertainties resulting from the choice of GEM profiles and from the calibration of τ represent biases and are thus not scaled by the effective degrees of freedom (Roessler et al., 2015). The uncertainties for the mean baroclinic transports are given in Table A2. Uncertainties range from 7.5 Sv to 8.8 Sv for the daily values and from 2.6 Sv to 2.9 Sv for the yearly mean values.

1. **Uncertainties in the τ measurements**

1a. Uncertainties due to sea roughness and rain: According to the manufacturer, for instrument depths of around 4,500 m, the standard deviation of a 24-ping sample is typically below 2.2 ms at wind speeds of 25 knots and in heavy rain around 3.5 ms, (University of Rhode Island, 2015). Using the larger value of 3.5 ms, this leads to a standard deviation of 0.7 ms for the daily mean travel times (Chidichimo et al., 2014; Roessler et al., 2015; University of Rhode Island, 2015).
Combined with the slope of the fit of the Fofonoff potential in Figure A1, this translates into an uncertainty between 1.1 Sv and 1.3 Sv for the daily values and between 0.06 Sv and 0.08 Sv for yearly mean values.

1b. The scatter from the linear relation between the Fofonoff potential χ and τ_{1900} is represented by the standard error Sε of the linear fit (Figure A1) which is for the daily values $3.2{\cdot}10^5$ J/m^2 for BP12 and $6.5{\cdot}10^5$ J/m^2 for the eastern PIES corresponding to error estimates ranging from 4.6 Sv to 5.8 Sv for the daily values and from 0.3 Sv to 0.4 Sv for the yearly mean values.

1c. The uncertainty originating in the CTD calibration of the measured τ into τ_{1900} includes uncertainties originating from i) the conversion of the measured τ into τ_{1900} and ii) the determination of the PIES depth.

i. For every PIES, the standard deviations of the correction factor to convert the measured τ into τ_{4500} and τ_{4100} is calculated. Then, the standard error of the fit is used as an estimator of the scatter of the fit translating into the uncertainty due to the conversion of τ_{4500} and τ_{4100} into τ_{1900}.

ii. The uncertainty in the determination of the instrument depth is calculated via error propagation from the standard deviation of the determined pressure at the instrument's depth.

The square root of the summed up squared individual uncertainties is then used as the total uncertainty related to the calibration procedure. The uncertainties range from 1.8 Sv to 2 Sv for the daily and yearly mean values since in this case the daily uncertainty is not scaled with the effective degree of freedom.

1d. The uncertainty in the baroclinic transport which results from the removal of the barotropic component of the travel time is estimated by taking into account the measurement accuracy of the half-hourly individual pressure measurements related to the removal of the drift in the pressure sensor procedure as described by Watts and Kontoyiannis (1990) who find an uncertainty of less than 0.02 dbar for de-drifted pressure time series that are at least a year long. Since the pressure time series used for this analysis consists of de-drifted and de-tided statistically independent daily mean values, the uncertainty of 0.02 dbar is divided by the effective degrees of freedom ($n = 48$) of a 24 h pressure record. This value is then converted into an equivalent of the acoustic travel time of 0.004 ms (for all PIES). The uncertainties range from 0.006 Sv to 0.007 Sv for the daily values and from 0.0003 Sv to 0.0004 Sv

For the total τ related transport uncertainty, all four uncertainties are combined by taking the square root of the sum of the individual squared uncertainties and multiplying the result with $\sqrt{2}$ since data from two PIES are used to two calculate the transport for a section. The total uncertainty for the baroclinic transports ranges from 7.2 Sv to 8.8 Sv for the daily values and from 2.6 Sv to 2.9 Sv for the yearly mean values.

2. Uncertainties in the creation of the GEM look-up table

The uncertainty of the calculated transports based on choice and availability of Argo float and shipboard CTD profiles is estimated by doing a bootstrapping analysis following Roessler et al. (2015). From the set of Argo float and shipboard CTD profiles that is used to create the GEM look-up table, the same number of profiles were drawn randomly with replacement. This procedure was repeated 1,000 times. For every new set of profiles, a transfer function and transports were calculated. The mean of the standard deviation at

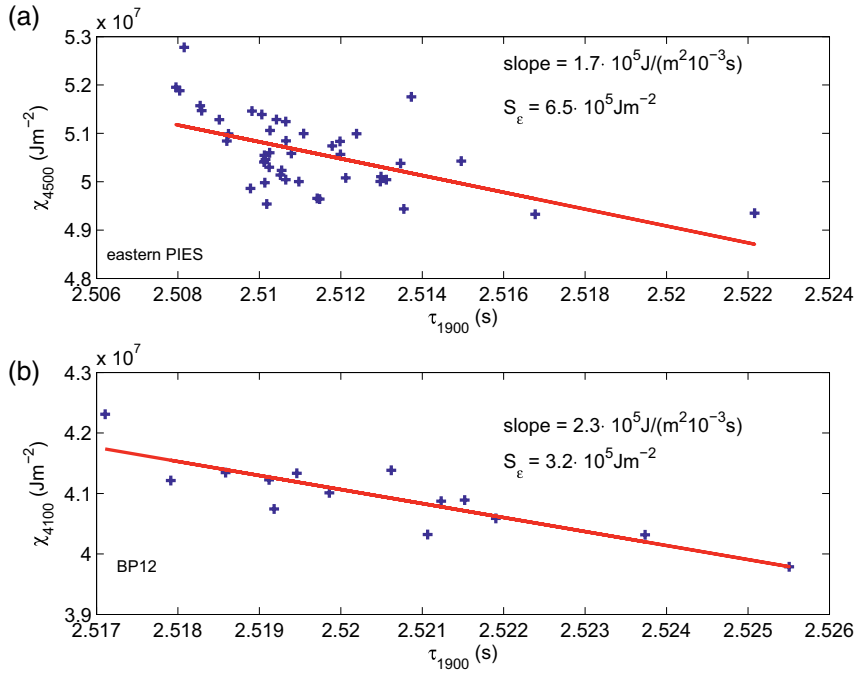

Figure A1. Fofonoff potential for CTD profiles used to create the transfer function with corresponding τ_{1900} values for (a) eastern basin PIES and (b) BP12. The Fofonoff potential X represents the potential energy anomaly and is defined as $X = g^{-1} \int p \cdot \mathrm{SVA}\, dp$ (with g being gravitational acceleration, p pressure and SVA specific volume anomaly). The scatter of the linear relation is expressed as the standard error of the fit. The slope of the fit is used to convert uncertainties in τ into uncertainties in Sverdrup (Meinen et al., 2004; Roessler et al., 2015).

Table A1
Effective degrees of freedom for the individual time series, used to estimate yearly uncertainties

	NAC Central (BP34 – BP12)	NAC East 1 (BP33 – BP34)	NAC East 2 (BP32 – BP33)
Baroclinic transport time series	15	17	14
Barotropic transport time series	40	27	26
Altimeter-based expanded transport	11	11	11

each time step was calculated and used as an uncertainty estimate. The estimates range from 0.002 Sv to 0.003 Sv for the daily and yearly mean values since again this uncertainty represents a bias error and is not scaled with the effective degree of freedom.

3. Uncertainties due to latitudinal differences between the PIES positions

The uncertainties resulting from the different latitudes of the deployment sites is estimated following Roessler et al. (2015): The difference between the maximal and minimal τ measured for each section is multiplied by the slope of the fit (Figure A1) divided by the mean density and the two different values for the Coriolis parameter respectively. This results in a maximal transport estimate due to the maximal difference in τ combined with an estimate for the impact of the change in the Coriolis parameter. The standard deviation of these two transport estimates represents the maximal and thus threefold standard deviation since it is based on the maximal τ difference. It is therefore divided by three to be comparable with the other estimated uncertainties. The resulting uncertainty estimates range from 0.02 Sv to 2.1 Sv for the daily values and from 0.0009 Sv to 0.1 Sv for the yearly mean values.

Total Uncertainty

To summarize, the total uncertainty estimates for the baroclinic transport as calculated from the square root of the sum of the squared errors accounting for the uncertainty in τ, the GEM profile choice and the latitudinal differences range from 7.5 Sv to 8.8 Sv for the daily values and from 2.6 Sv to 2.9 Sv for the yearly averages.

A2 Uncertainties in the Altimeter-Based Extended Transport Time Series

Following Roessler et al. (2015) the uncertainty in the daily altimeter-based extended transport is calculated from the mean standard deviation of the residuals between the altimetry based absolute baroclinic transport time series and the absolute baroclinic transport calculated from the PIES (2.2 Sv–2.3 Sv for the daily values).

To obtain an estimate of the uncertainty of the annual means, the uncertainty for the daily values is scaled with the effective degree of freedom calculated from the integral time scale. Typical integral time scales for the altimeter expanded time series for one year of data are in the range of 16–32 days. To not underestimate the decorrelation time scale we choose the maximal time of 32 days for scaling the uncertainty of the daily values and obtain an uncertainty estimate for the annual mean values of 0.2 Sv for all sections.

Combined with the uncertainties in the PIES transports this yields a total uncertainty of 7.8 Sv–9.1 Sv for the daily transport times series and 2.6 Sv–2.9 Sv for the yearly time series (Table A2).

Table A2
Summary of the estimated daily (first value) and, if applicable, yearly (second value) uncertainties which are obtained by scaling the daily value with the effective degree of freedom (cf. Table A1) for the individual sections. The uncertainties due to the CTD calibration and the GEM profile choice are not scaled with the effective degree of freedom thus the yearly uncertainty estimate corresponds to the daily uncertainty estimate (Roessler et al., 2015). Uncertainties are given in Sverdrup.

			NAC Central	NAC East 1	NAC East 2
Barotropic transport			1.2/0.03	1.6/0.06	1.7/0.06
Baroclinic transport	τ	Sea roughness/rain	1.3/0.08	1.1/0.06	1.1/0.08
		Scatter from linear fit	4.6/0.3	5.8/0.3	5.8/0.4
		CTD Calibration	1.8/-	2.0/-	2.0/-
		Removal of barotropic part	0.007/0.0004	0.006/0.0003	0.006/0.0004
		Total	7.2/2.6	8.8/2.9	8.7/2.8
	GEM profile choice		0.003/-	0.002/-	0.002/-
	Coriolis parameter		2.1/0.1	0.02/0.0009	0.02/0.001
	Total		7.5/2.6	8.8/2.9	8.7/2.8
Altimeter-based extended transport			2.2/0.2	2.2/0.2	2.3/0.2
Total			7.8/2.6	9.1/2.9	9.0/2.9

CTD, conductivity-temperature-depth; NAC, North Atlantic Current.

Data Availability Statement

The NCEP/NCAR reanalysis data were provided by the NOAA/OAR/ESRL PSL, Boulder, Colorado, USA, and were downloaded from their web site at psl.noaa.gov/data/gridded/data.ncep.reanalysis.surfaceflux.html on June 11, 2020. The Argo float data (Argo, 2002) were collected and made freely available by the International Argo Program and the national programs that contribute to it (http://www.argo.ucsd.edu, http://argo.jcommops.org). The Argo program is part of the Global Ocean Observing System. The authors thank Birgit Klein, Federal Maritime and Hydrographic Agency (BSH), Hamburg, Germany, for kindly providing quality-controlled Argo data from the North Atlantic, which were downloaded July 17, 2018 (https://doi.org/10.17882/42182#58010). The research cruise CE17007 (2017) was carried out with the support of the Marine Institute and funded under the Marine Research Program 2014–2020 by the Irish Government. The authors thank Pascale Lherminier (Ifremer, France) for providing the CTD data of the cruises BOCATS (2016) and OVIDE (2018). Detailed information on the PIES, CTD and LADCP data for the MAR region can be found in Roessler et al. (2015) and for the western basin in Rhein et al. (2019). The CTD data from the RV Maria S. Merian research cruises are available from PANGAEA (MSM43: doi.org/10.1594/PANGAEA.897988, MSM53 doi.org/10.1594/PANGAEA.910842, MSM64: doi.org/10.1594/PANGAEA.923550, MSM73: doi.org/10.1594/PANGAEA.923565). The PIES travel time and pressure fluctuation data for the eastern basin and additional data from the MAR region (doi.org/10.1594/PANGAEA.925118) as well as additional LADCP data for the eastern basin (doi.org/10.1594/PANGAEA.922859) are also available from PANGAEA.

Acknowledgments
H. Nowitzki was funded by the German Science Foundation (DFG) through the International Research Training Group ArcTrain "Processes and impacts of climate change in the North Atlantic Ocean and the Canadian Arctic" (IRTG 1904 ArcTrain to M. Rhein). The shipboard and moored data at 47°/48°N—the NOAC array—are part of the North Atlantic/RACE programs funded by the German Ministry of Education and Research (Grants 03F0443C, 03F0605C, 03F0561C, and 03F0792A to M. Rhein). The Senate Commission of Oceanography of the DFG granted ship time and funds for logistics and consumables (to M. Rhein and D. Kieke). The assistance and technical support from the ship crew of RV Maria S. Merian are gratefully acknowledged. R. Steinfeldt (IUP-MARUM, University Bremen, Germany) was responsible for the calibration of all NOAC CTD data used to calculate the GEMS. The study has been conducted using E.U. Copernicus Marine Service Information (product identifier: SEALEVEL_GLO_PHY_L4_REP_OBSERVATIONS_008_047). The authors also thank the anonymous reviewers for their valuable comments that helped to improve the manuscript. Open access funding enabled and organized by Projekt DEAL.

References

Amante, C., & Eakins, B. W. (2009). *ETOPO1 1 Arc-Minute global relief model: Procedures, data sources and analysis*. NOAA Technical Memorandum NESDIS NGDC-24 National Geophysical Data Center, NOAA. https://doi.org/10.7289/V5C8276M

Argo (2002). *Argo float data and metadata from global data assembly centre (Argo GDAC)*. SEANOE. Retrieved from https://doi.org/10.17882/42182

Bayley, G. V., & Hammersley, J. M. (1946). The "effective" number of independent observations in an autocorrelated time series. *Supplement to the Journal of the Royal Statistical Society*, *8*(2), 184–197. https://doi.org/10.2307/2983560

Bower, A. S., Lozier, M. S., Gary, S. F., & Böning, C. W. (2009). Interior pathways of the North Atlantic meridional overturning circulation. *Nature*, *459*(7244), 243–247. https://doi.org/10.1038/nature07979

Bower, A. S., & von Appen, W.-J. (2008). Interannual variability in the pathways of the North Atlantic Current over the Mid-Atlantic ridge and the impact of topography. *Journal of Physical Oceanography*, *38*(1), 104–120. https://doi.org/10.1175/2007JPO3686.1

Breckenfelder, T., Rhein, M., Roessler, A., Böning, C. W., Biastoch, A., Behrens, E., & Mertens, C. (2017). Flow paths and variability of the North Atlantic Current: A comparison of observations and a high-resolution model. *Journal of Geophysical Research: Oceans*, *122*, 2686–2708. https://doi.org/10.1002/2016JC012444

Chaplin, G. F., & Watts, D. R. (1984). *Inverted Echo Sounder Development* in OCEANS 1984 (pp. 249–253). Marine Technology Society, Washington, DC. https://doi.org/10.1109/OCEANS.1984.1152347

Chidichimo, M. P., Donohue, K. A., Watts, D. R., & Tracey, K. L. (2014). Baroclinic transport time series of the Antarctic circumpolar current measured in drake passage. *Journal of Physical Oceanography*, *44*(7), 1829–1853. https://doi.org/10.1175/JPO-D-13-071.1

Daniault, N., Mercier, H., Lherminier, P., Sarafanov, A., Falina, A., Zunino, P., et al. (2016). The northern North Atlantic ocean mean circulation in the early 21st century. *Progress in Oceanography*, *146*, 142–158. https://doi.org/10.1016/j.pocean.2016.06.007

Del Grosso, V. A. (1974). New equation for the speed of sound in natural waters (with comparisons to other equations). *Journal of the Acoustical Society of America*, *56*(4), 1084–1091. https://doi.org/10.1121/1.1903388

Ellett, D. J., & Martin, J. H. A. (1973). The physical and chemical oceanography of the Rockall channel. *Deep-Sea Research and Oceanographic Abstracts*, *20*(7), 585–588. https://doi.org/10.1016/0011-7471(73)90030-2

Frajka-Williams, E., Ansorge, I. J., Baehr, J., Bryden, H. L., Chidichimo, M. P., Cunningham, S. A., et al. (2019). Atlantic meridional overturning circulation: Observed transport and variability. *Frontiers in Marine Science*, *6*, 260. https://doi.org/10.3389/fmars.2019.00260

García-Ibáñez, M. I., Pardo, P. C., Carracedo, L. I., Mercier, H., Lherminier, P., Ríos, A. F., & Pérez, F. F. (2015). Structure, transports and transformations of the water masses in the Atlantic Subpolar Gyre. *Progress in Oceanography*, *135*, 18–36. https://doi.org/10.1016/j.pocean.2015.03.009

Garrett, & Petrie (1981). Dynamical Aspects of the Flow Through the Strait of Belle Isle. *Journal of Physical Oceanography*, *11*, 376–393. https://doi.org/10.1175/1520-0485(1981)011<0376:DAOTFT>2.0.CO;2

González-Pola, C., Larsen, K. M. H., Fratantoni, P., & Beszczynska-Möller, A. (Eds.), (2019). *ICES Report on Ocean Climate 2018*. ICES Cooperative Research Report No. 349. https://doi.org/10.17895/ices.pub.5461

González-Pola, C., Lavín, A., & Vargas-Yáñez, M. (2005). Intense warming and salinity modification of intermediate water masses in the southeastern corner of the Bay of Biscay for the period 1992–2003. *Journal of Geophysical Research*, *110*(5), 1–14. https://doi.org/10.1029/2004JC002367

Häkkinen, S., Rhines, P. B., & Worthen, D. L. (2016). Warming of the global ocean: Spatial structure and water-mass trends. *Journal of Climate*, *29*(13), 4949–4963. https://doi.org/10.1175/JCLI-D-15-0607.1

Hallock (1987). Regional characteristics for interpreting inverted echo sounders (IES) Observations. *Journal of Atmospheric and Oceanic*, *4*, 298–304. https://doi.org/10.1175/1520-0426(1987)004<0298:RCFIIE>2.0.CO;2

He, Y., Watts, D. R., & Tracey, K. L. (1998). Determining geostrophic velocity shear profiles with inverted echo sounders. *Journal of Geophysical Research*, *103*(C3), 5607–5622. https://doi.org/10.1029/97JC03439

Holliday, N. P., Bersch, M., Berx, B., Chafik, L., Cunningham, S., Florindo-López, C., et al. (2020). Ocean circulation causes the largest freshening event for 120 years in eastern subpolar North Atlantic. *Nature Communications*, *11*(1), 1–15. https://doi.org/10.1038/s41467-020-14474-y

Holliday, N. P., Cunningham, S. A., Johnson, C., Gary, S. F., Griffiths, C., Read, J. F., & Sherwin, T. (2015). Multidecadal variability of potential temperature, salinity and transport in the eastern subpolar North Atlantic. *Journal of Geophysical Research: Oceans*, *120*, 5945–5967. https://doi.org/10.1002/2015JC010762

Huthnance, J. (1986). The Rockall slope current and shelf-edge processes. *Proceedings of the Royal Society of Edinburgh-Section B: Biological Sciences*, *88*, 83–101. https://doi.org/10.1017/S0269727000004486

Iorga, M. C., & Lozier, M. S. (1999). Signatures of the Mediterranean outflow from a North Atlantic climatology 1. Salinity and density fields. *Journal of Geophysical Research: Oceans*, *104*(C11), 26011–26029. https://doi.org/10.1029/1999JC900115

Intergovernmental Panel on Climate Change. (2014). *Climate Change 2013 – The Physical Science Basis: Working Group I Contribution to the Fifth Assessment Report of the Intergovernmental Panel on Climate Change*. Cambridge: Cambridge University Press. https://doi.org/10.1017/CBO9781107415324

Kalnay, E., Kanamitsu, M., Kistler, R., Collins, W., Deaven, D., Gandin, L., & Joseph, D. (1996). The NCEP/NCAR 40-Year Reanalysis Project. *Bulletin of the American Meteorological Society*, *77*, 437–472. https://doi.org/10.1175/1520-0477(1996)077<0437:TNYRP>2.0.CO;2

Kieke, D., Klein, B., Stramma, L., Rhein, M., & Koltermann, K. P. (2009). Variability and propagation of Labrador Sea Water in the southern subpolar North Atlantic. *Deep-Sea Research I*, *56*, 1656–1674. https://doi.org/10.1016/j.dsr.2009.05.010

Kwon, Y. O., & Riser, S. C. (2005). General circulation of the western subtropical North Atlantic observed using profiling floats. *Journal of Geophysical Research*, *110*(10), 1–22. https://doi.org/10.1029/2005JC002909

Lherminier, P. (2018). *OVIDE 2018 cruise*. RV Thalassa. https://doi.org/10.17600/18000510

Lherminier, P., Mercier, H., Huck, T., Gourcuff, C., Perez, F. F., Morin, P., et al. (2010). The Atlantic meridional overturning circulation and the subpolar gyre observed at the A25-OVIDE section in June 2002 and 2004. *Deep-Sea Research Part I: Oceanographic Research Papers*, *57*(11), 1374–1391. https://doi.org/10.1016/j.dsr.2010.07.009

Lozier, M. S., & Stewart, N. M. (2008). On the temporally varying northward penetration of Mediterranean overflow water and eastward penetration of Labrador sea water. *Journal of Physical Oceanography*, *38*(9), 2097–2103. https://doi.org/10.1175/2008JPO3908.1

McCarthy, G. D., Brown, P. J., Flagg, C. N., Goni, G., Houpert, L., Hughes, C. W., et al. (2020). Sustainable observations of the AMOC: Methodology and technology. *Reviews of Geophysics*, *58*, e2019RG000654. https://doi.org/10.1029/2019RG000654

Meinen, C. S., Garzoli, S. L., Johns, W. E., & Baringer, M. O. (2004). Transport variability of the Deep Western Boundary Current and the Antilles Current off Abaco Island, Bahamas. *Deep-Sea Research I*, *51*, 1397–1415. https://doi.org/10.1016/j.dsr.2004.07.007

Meinen, C. S., & Watts, D. R. (1998). Calibrating Inverted Echo Sounders Equipped with Pressure Sensors. *Journal of Atmospheric and Oceanic Technology*, *15*, 1339–1345. https://doi.org/10.1175/1520-0426(1998)015<1339:CIESEW>2.0.CO;2

Meinen, C. S., & Watts, D. R. (2000). Vertical structure and transport on a transect across the North Atlantic Current near 42°N: Time series and mean. *Journal of Geophysical Research*, *105*(C9), 21869–21891. https://doi.org/10.1029/2000JC900097

Mercier, H., Lherminier, P., Sarafanov, A., Gaillard, F., Daniault, N., Desbruyères, D., et al. (2015). Variability of the meridional overturning circulation at the Greenland-Portugal OVIDE section from 1993 to 2010. *Progress in Oceanography*, *132*, 250–261. https://doi.org/10.1016/j.pocean.2013.11.001

Mertens, C., Rhein, M., Walter, M., Böning, C. W., Behrens, E., Kieke, D., et al. (2014). Circulation and transports in the Newfoundland Basin, western subpolar North Atlantic. *Journal of Geophysical Research: Oceans*, *119*, 7772–7793. https://doi.org/10.1002/2014JC010019

Østerhus, S., Woodgate, R., Valdimarsson, H., Turrell, B., De Steur, L., Quadfasel, D., et al. (2019). Arctic Mediterranean exchanges: A consistent volume budget and trends in transports from two decades of observations. *Ocean Science*, *15*(2), 379–399. https://doi.org/10.5194/os-15-379-2019

Perez, F. F., Fontela, M., García-Ibáñez, M. I., Mercier, H., Velo, A., Lherminier, P., et al. (2018). Meridional overturning circulation conveys fast acidification to the deep Atlantic Ocean. *Nature*, *554*, 515–518. https://doi.org/10.1038/nature25493

Reid, J. L. (1979). On the contribution of the Mediterranean Sea outflow to the Norwegian-Greenland Sea. *Deep Sea Research Part A: Oceanographic Research Papers*, *26*(11), 1199–1223. https://doi.org/10.1016/0198-0149(79)90064-5

Rhein, M., Kieke, D., Hüttl-Kabus, S., Roessler, A., Mertens, C., Meissner, R., & Yashayaev, I. (2011). Deep water formation, the subpolar gyre, and the meridional overturning circulation in the subpolar North Atlantic. *Deep-Sea Research II*, *58*, 1819–1832. https://doi.org/10.1016/j.dsr2.2010.10.061

Rhein, M., Mertens, C., & Roessler, A. (2019). Observed transport decline at 47°N, Western Atlantic. *Journal of Geophysical Research: Oceans*, *124*(7), 4875–4890. https://doi.org/10.1029/2019JC014993

Roessler, A., Rhein, M., Kieke, D., & Mertens, C. (2015). Long-term observations of North Atlantic Current transport at the gateway between western and eastern Atlantic. *Journal of Geophysical Research: Oceans*, *120*, 4003–4027. https://doi.org/10.1002/2014JC010662

Rossby, T. (1996). The North Atlantic Current and surrounding waters: At the crossroads. *Reviews of Geophysics*, *34*(4), 463–481. https://doi.org/10.1029/96RG02214

Schmitz, W. J., & McCartney, M. S. (1993). On the North Atlantic circulation. *Reviews of Geophysics*, *31*(1), 29–49. https://doi.org/10.1029/92RG02583

Schneider, L., Kieke, D., Jochumsen, K., Colbourne, E., Yashayaev, I., Steinfeldt, R., et al. (2015). Variability of Labrador Sea water transported through Flemish Pass during 1993–2013. *Journal of Geophysical Research: Oceans*, *120*(8), 5514–5533. https://doi.org/10.1002/2015JC010939

Schott, Zantopp, Stramma, Dengler, Fischer, & Wibaux (2004). Circulation and deep-water export at the Western exit of the subpolar North Atlantic. *Journal of Physical Oceanography*, *34*, 817–843. https://doi.org/10.1175/1520-0485(2004)034<0817:CADEAT>2.0.CO;2

Stendardo, I., Kieke, D., Rhein, M., Gruber, N., & Steinfeldt, R. (2015). Interannual to decadal oxygen variability in the mid-depth water masses of the eastern North Atlantic. *Deep-Sea Research Part I: Oceanographic Research Papers*, *95*, 85–98. https://doi.org/10.1016/j.dsr.2014.10.009

Stendardo, I., Rhein, M., & Steinfeldt, R. (2020). The North Atlantic Current and its volume and freshwater transports in the subpolar North Atlantic, time period 1993–2016. *Journal of Geophysical Research: Oceans*, *125*, e2020JC016065. https://doi.org/10.1029/2020JC016065

Teague, W. J., Hallock, Z. R., Jacobs, G. A., & Mitchell, J. L. (1995). Kuroshio sea surface height fluctuations observed simultaneously with inverted echo sounders and TOPEX/POSEIDON. *Journal of Geophysical Research*, *100*(C12), 24987–24994. https://doi.org/10.1029/95JC01526

University of Rhode Island. (2015). *Inverted echo sounder user's manual IES model 6.2C*. Narragansett.

van Aken, H. M., & Becker, G. (1996). Hydrography and through-flow in the north-eastern North Atlantic Ocean: the NANSEN project. *Progress in Oceanography*, *38*, 297–346. https://doi.org/10.1016/S0079-6611(97)00005-0

Watts, & Kontoyiannis (1990). Deep-ocean bottom pressure measurement: Drift removal and performance. *Journal of Atmospheric and Oceanic Technology*, *7*, 296–306. https://doi.org/10.1175/1520-0426(1990)007<0296:DOBPMD>2.0.CO;2

Watts, & Rossby (1977). Measuring Dynamic Heights with Inverted Echo Sounders: Results from MODE. *Journal of Physical Oceanography*, *7*, 345–358. https://doi.org/10.1175/1520-0485(1977)007<0345:MDHWIE>2.0.CO;2

Watts, D. R., Sun, C., & Rintoul, S. (2001). A two-dimensional gravest empirical mode determined from hydrographic observations in the Subantarctic front. *Journal of Physical Oceanography*, *31*, 2186–2209. https://doi.org/10.1175/1520-0485(2001)031<2186:ATDGEM>2.0.CO;2